High-efficiency, low-loss Floquet Josephson Traveling Wave Parametric Amplifier

by

Jennifer Wang

B.A., Wellesley College (2020)

Submitted to the Department of Electrical Engineering and Computer Science
in partial fulfillment of the requirements for the degree of

MASTER OF SCIENCE

at the

MASSACHUSETTS INSTITUTE OF TECHNOLOGY

May 2025

Authored by: Jennifer Wang
Department of Electrical Engineering and Computer Science
April 25, 2025

Certified by: Kevin P. O'Brien
Associate Professor of Electrical Engineering and Computer Science
Thesis Supervisor

Accepted by: Leslie A. Kolodziejski
Professor of Electrical Engineering and Computer Science
Chair, Department Committee on Graduate Students

High-efficiency, low-loss Floquet Josephson Traveling Wave Parametric Amplifier

by

Jennifer Wang

Submitted to the Department of Electrical Engineering and Computer Science
on April 25, 2025, in partial fulfillment of the
requirements for the degree of
MASTER OF SCIENCE

Abstract

Advancing error-corrected quantum computing and fundamental science necessitates quantum-limited amplifiers with near-ideal quantum efficiency and multiplexing capability. However, existing solutions achieve one at the expense of the other; for example, Josephson traveling wave parametric amplifiers (JTWPAs) are high-gain, broadband, and chip-based quantum amplifiers that conventionally incur a bandwidth-noise tradeoff. When operated at 20-dB gain and instantaneous bandwidths of a few GHz, JTWPAs typically reach near-quantum limited intrinsic efficiencies of 70% - 85% relative to that of an ideal phase-preserving quantum amplifier. This is due to information leakage to the sidebands of the JTWPA, which can be recovered by adiabatically transforming the input modes to Floquet modes of the system within the device.

In this thesis, we experimentally demonstrate the first Floquet-mode traveling-wave parametric amplifier (Floquet TWPA). Fabricated in a superconducting qubit process, this Floquet TWPA achieves minimal dissipation, quantum-limited noise performance, and broadband operation. Our device exhibits $>$ 20-dB amplification over a 3-GHz instantaneous bandwidth, <0.5-dB average in-band insertion loss, and the highest-reported intrinsic quantum efficiency for a TWPA of $92.1 \pm 7.6\%$, relative to an ideal phase-preserving amplifier. When measuring a superconducting qubit, our Floquet TWPA enables a system measurement efficiency of $65.1 \pm 5.8\%$, the highest-reported in a superconducting qubit readout experiment utilizing phase-preserving amplifiers to the best of our knowledge. Finally, we discuss the noise limitations of our current experimental setup, as well as impedance matching strategies that will enable us to push towards ideal JTWPA performance. These general-purpose Floquet TWPAs are suitable for fast, high-fidelity multiplexed readout in large-scale quantum systems and future monolithic integration with quantum processors.

Thesis Supervisor: Kevin P. O'Brien
Title: Associate Professor of Electrical Engineering and Computer Science

Acknowledgments

The work in this thesis would not have been possible without the help and guidance of many colleagues and friends.

First and foremost, I would like to thank my advisor, Professor Kevin O'Brien, for sharing his time, expertise, and advice throughout my time in QCE. When I first joined Kevin's group (with no experience in electrical engineering), writing a thesis like this was a daunting prospect. Kevin's hands-on mentorship in everything from designing circuits to electromagnetic simulations to debugging measurement chains made it a reality. Beyond the technical, I am lucky to be able to depend on Kevin for guidance and support as I navigate becoming a part of the vibrant quantum electronics research community, and his leadership has made QCE a warm and supportive academic home.

I'm also especially grateful for the support and collaboration of Kaidong Peng, co-first-author of the paper which grew out of the work in this thesis, as well as designer of this first Floquet TWPA. Since I started as a graduate student, Kaidong been a dedicated and patient mentor. He taught me about everything from foundational principles in nonlinear optics to nitty-gritty computational techniques, helped me acquire the tacit knowledge of how to do good lab work, and continues to inspire me with his optimistic and tireless dedication to our scientific mission.

Furthermore, I deeply appreciate the expertise of knowledgeable and generous MIT staff over these years. I am honored to work with many collaborators at MIT Lincoln Laboratory who fabricated the Floquet TWPA device: Jeffrey M. Knecht, Michael Gingras, Bethany M. Niedzielski, Hannah Stickler, Katrina Sliwa, Kyle Serniak, and Mollie E. Schwartz. In addition to providing innovative technical expertise and precise fabrication processes, they have also been incredibly patient and flexible with the development of this project, as well as genuine friends outside of work; I could not ask for better collaborators. On campus, I would like to thank Professor William Oliver, who helped originate the idea of Floquet TWPAs fabricated in a qubit process, provided the wQED device designed by Aziza Almanakly, and continues to offer

essential support to QCE in our scientific journey. I am also grateful to Professor Karl Berggren for sage advice about my PhD goals, and Dr. Steven Nagle for his resourceful and generous help with developing packages in the Rodgers lab.

My lab members have made the past few years very special; many thanks to Madhi Naghiloo, Kaidong Peng, Bright Ye, and Greg Cunningham for welcoming me to QCE, and I really enjoy getting to know Alec Yen, Jessica Kedziora, Daniela Zaidenberg, Andres Lombo, Jeremy Kline, and Eric Bui. They are all brilliant people with a diverse array of interests, and they are always ready to offer advice, cameraderie, and occasionally ridiculous conversational topics. Special thanks to the TWPA team for solidarity during hours of late-night lab work, Jessica for expert advice and crazy life stories, as well as Greg and Alec for the best office vibes. In addition, I would like to thank Wouter Van De Pontseele, Mingyu (Charles) Li, Jiatong Yang, and Professor Joe Formaggio for not only welcoming me as a potential collaborator on the Project 8 neutrino mass measurement experiment, but also being delightful people to hang out on grueling hikes with.

My friends are indispensable to my life and keep me grounded to the world beyond academia. Maddy, Lynne, Mar, Shana, Perrin, Matt, and Hana have kept me sane throughout college and the early days of the pandemic; I am so excited to grow alongside you and cheer on everyone's accomplishments. Many thanks also to all the graduate students and postdocs who have mentored for my outreach program, QuERY; I am deeply grateful to meet so many inspiring scientists who share the same vision and dedication to science communication.

To those I have lost during the pandemic: Han Gui Fen, Wang En Zeng, Feng Guang Yu, and Alexander Rubin; I will always remember you and cherish the time we had together.

Last but not least, I would not be here today without my parents, who first encouraged me to pursue science. My partner, Robert Jones, has been a loving and constant anchor for the past four years, and I truly feel at home with the Jones family. I am beyond lucky to share my life with you all.

Contents

List of Figures

Chapter 1

Introduction

Quantum-limited amplifiers enable faithful detection of single-photon-level signals by noisy real-world electronics [8]. They are critical front-end hardware for various information-critical applications in quantum information science, metrology, and astronomy. Since their development, quantum-limited amplifiers have enabled fast and high-fidelity single-shot readout of quantum bit (qubit) states [9, 10] and will continue to play an increasingly important role in the era of fault-tolerant quantum computing. Due to algorithmic complexity, finite qubit coherence, and imperfect hardware control [11], large-scale quantum computers with potentially millions of physical qubits and active quantum error correction are needed to ensure fault-tolerant operations and empower real-world applications.

Surface codes [12, 13, 14, 15] are leading quantum error correction (QEC) schemes due to their high error threshold, compatibility with 2D hardware architectures, and the availability of efficient error decoding algorithms [16, 17]. In each QEC cycle, physical qubit errors are detected and decoded by sets of simultaneous stabilizer measurements on auxiliary qubits to extract the error syndromes of data qubits, without collapsing the underlying logical qubit state. For QEC to break even and improve the overall error rate, surface codes thus require quantum-limited amplifiers, which enable real-time quantum feedback as well as minimize both the readout errors and the error-correction cycle duration to reduce qubit decoherence. Additionally, the logical state preparation error also depends on the readout speed and fidelity of the

corresponding initialization stabilizer measurements. Fast, high-fidelity readout is thus critical to the success of QEC, which imposes stringent performance and scalability requirements on the measurement hardware, especially the quantum-limited preamplifiers.

Josephson traveling-wave parametric amplifiers (JTWPAs) [18, 19, 20, 21, 22] are promising candidates as quantum preamplifiers for large-scale fault-tolerant quantum computers. JTWPAs achieve near-quantum-limited noise performance over several gigahertz of instantaneous bandwidth and a high dynamic range (-80 to -110 dBm), capable of simultaneously reading out tens to hundreds of frequency-multiplexed qubits. However, JTWPAs introduce more noise than resonator-based amplifiers [23, 24, 25, 26, 27, 28] due to non-negligible material loss and coherent sideband leakage [18, 7], leading to either degraded readout fidelity or extended measurement time.

Floquet-mode traveling-wave parametric amplifiers (Floquet TWPAs) [7] have recently been proposed to overcome the quantum efficiency-bandwidth trade-off in conventional TWPAs. In comparison, Floquet TWPAs encode information in instantaneous Floquet modes rather than single-frequency modes to eliminate sideband leakage from parasitic nonlinear processes. Furthermore, Floquet TWPAs adiabatically mode-match the information-carrying Floquet modes to single-frequency modes for convenient usage, improved directionality, and insensitivity to out-of-band impedance mismatch, paving the way for direct integration with quantum processors without isolators.

Experimentally realizing Floquet TWPAs with these advantages is challenging, as they require greater electrical length and are consequently more vulnerable to material dissipation than conventional TWPAs. TWPAs are often implemented with parallel-plate capacitors using lossy dielectrics such as silicon oxide [18, 29] and alumina [20, 21] ($\tan\delta \approx 10^{-3}$). At this loss level, the intrinsic quantum efficiency of Floquet TWPAs will be limited by material loss and is predicted to decrease to $\sim 90\%$ [30] from 99.9% when lossless, diminishing the performance advantages over the conventional amplifier paradigm. Since the completion of this manuscript, we

have become aware of a recent preprint [31], which uses a superconducting-qubit fabrication process to implement a periodically-loaded JTWPA.

In this work, we present the first experimental demonstration of a Floquet TWPA, fabricated in a superconducting qubit process. In addition to simpler fabrication and integrability with superconducting qubits, our implementation dramatically reduces material loss by more than 50× compared to existing parallel-plate processes, using a single-layer defined distributed coplanar capacitors on a high-resistivity crystalline silicon substrate [1, 31]. Overall, our implementation results in an effective loss tangent $\tan\delta_{\text{eff}} \approx 6 \times 10^{-5}$ and $< 0.5\,\text{dB}$ of average insertion loss within the entire 4-12 GHz frequency range, dominated by packaging and impedance mismatch and can be further minimized with qubit-amplifier integration in the future. Our Floquet TWPA achieves a peak gain exceeding 20 dB, several gigahertz of instantaneous 3-dB bandwidth, and a 1-dB compression point of -106.5 dBm at 21 dB gain, making it suitable for use in large-scale fault-tolerant quantum computers and various other information-critical applications.

1.1 Thesis outline

This thesis is organized as follows. Chapter 2 provides background information on the historical development of the JTWPA and the need to optimize noise performance, scalability, and integrability, leading to the design of the Floquet TWPA. We examine the available pool of power calibration methods to evaluate amplifier performance and identify two in-situ methods, the waveguide QED (wQED) and circuit QED (cQED) calibrations that we utilize in this work. We then derive how to obtain the intrinsic of the Floquet TWPA and full-system of a measurement chain for qubit readout.

Chapter 3 reviews circuit quantum electrodynamics, focusing on a discussion of topics helpful for understanding the theoretical basis of JTWPAs. In particular, we discuss Josephson junctions and the quantum LC resonator, which provide crucial nonlinearity and serve as the fundamental building block for superconducting quantum devices. We then summarize the relevant theoretical background for JTWPAs,

including the nonlinear wave equation and phase matching strategies. This will provide useful intuition for the development of Floquet JTWPAs, and we will discuss how the performance of a JTWPA depends on phase matching and sideband losses.

Chapter 4 describes the device under study, fabricated by our collaborators at Lincoln Laboratory with a superconducting Al qubit process. Next, we present measurements of the gain, insertion loss, and P1dB of the aforementioned device. A comprehensive measurement setup diagram is provided in Appendix A. We implement packaging improvements that enable quick, modular and better impedance-matched measurements of the devices; further details are provided in Appendix B.

Chapter 5 reports on the intrinsic quantum efficiency of the Floquet TWPA. We measure a flux-tunable waveguide QED (wQED) device and perform a global fit over input-power-dependent transmission to define the absolute power calibration. Our obtained intrinsic quantum efficiency is the highest reported for a TWPA device to the best of our knowledge. We also discuss the concomitant susceptibility to self-oscillations that results from having near-ideal insertion loss.

Chapter 6 reports our full-system quantum efficiency characterization results for a qubit readout experiment utilizing the Floquet TWPA. Using measurement-induced dephasing of a circuit QED (cQED) superconducting qubit measured in reflection, we obtain a power calibration at the resonator frequency of the qubit, and demonstrate that the Floquet TWPA provides the highest full system quantum efficiency reported thus far for a phase-preserving amplifier. We perform qubit readout with this device acting as a preamplifier.

Finally, Chapter 7 concludes by discussing the limitations of our experimental setup and outlining future steps for the use of Floquet JTWPAs in fault-tolerant quantum computing experiments.

Chapter 2

Background and related work

Broadly speaking, the motivation for engineering JTWPA devices lies in faithful amplification of very small RF signals from cryogenic experiments. In particular, superconducting qubit experiments rely on a nonlinear element called the Josephson junction, which is a junction between two superconducting metal layers, to produce weakly correlated electron wavefunctions that can tunnel through the junction. These systems are engineered at radio and microwave frequencies to be compatible with widely-used semiconductor fabrication processes and commercially available measurement instrumentation [32]. However, since the temperature requirements for superconductivity are low, usually around 10 to 20 mK, achieving excellent qubit readout is quite difficult; retrieving a signal on the order of femtowatts and sending it back to room temperature introduces extra heating and therefore loss into the system. Moreover, since the qubits themselves decohere easily due to fabrication inconsistencies and coupling to the environment, so the input signal itself needs to be a weak tone. As discussed in Chapter 1, JTWPAs are often utilized in such experiments due to their relatively low noise and high broadband gain [33, 6, 2, 18, 21].

Another field with similar power requirements to superconducting qubit measurement is fundamental particle physics research. As more sensitive detectors such as quantum amplifiers have been developed, there has been increased interest in mid-scale experiments involving a measurement volume on the order of tens of cubic meters, instead of full particle colliders or Cherenkov detector tanks [34]. One such

example in neutrino mass measurement is Project 8, which involves precisely detecting coherent cyclotron radiation from electrons emitted in the beta decay of a gaseous source in a large magnetic field. The cyclotron frequency depends on the electron's kinetic energy because of relativistic effects, which can be then used to reconstruct the mass of the neutrino [34]. This approach is advantageous since its sensitivity scales with detector volume, it is less sensitive to systematic uncertainty, and the extracted measurement is model-independent; however, at a magnetic field of 1T, the 26 GHz cyclotron radiation is only about 1 femtowatt in power [34], similar to the power requirements and readout challenges involved in a superconducting qubit readout experiment. This requires a signal-to-noise ratio 10 to 20 times greater than currently achieved per receiver antenna with commercial off-the-shelf amplifiers, and we need to trigger the signal within 10 microseconds to achieve the desired energy resolution. Hence, the low-noise, tunable, and high-gain JTWPA can also be tailored for this application.

In addition to neutrino mass measurement, another popular application of quantum amplifiers is the detection of dark matter. Proposed haloscopes often have similarities with the Project 8 neutrino mass detection process, utilizing a resonant cavity and a large magnetic field (around 8 Telsa) to detect very weak conversion events of dark matter axions into microwave photons. The recent work by ADMX is a first demonstration of a JTWPA-aided resonant cavity haloscope dark matter search, which has already eliminated one of the two axion benchmark models from 1.9 μeV to 3.53 μeV, and currently working towards discovering 2 μeV to 20 μeV dark matter axions within the next 10 years [35]. On a larger scale, the Vinante group has recently proposed to create detector arrays with both JTWPAs and kinetic inductance TWPAs, with the aim of creating general detectors useful not only for dark matter and neutrino detection, but also for CMB and next-generation X-ray measurements [36].

To explore why JTWPAs are such an attractive choice for high sensitivity experiments, we start first with the Friis formula to evaluate the total noise of a measurement chain, which is depicted in Fig. 2-1. In this chain, a source is amplified by N

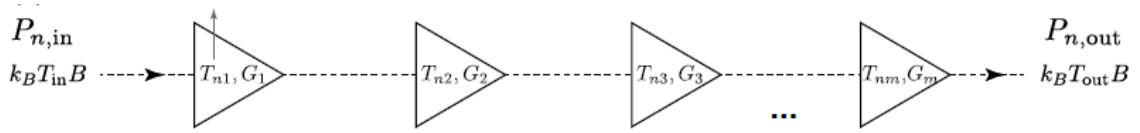

Figure 2-1: Simplified measurement chain featuring multiple amplifiers, adapted from [1]. The Friis equation indicates that the noise temperature of the first amplifier in the chain dominates the overall output noise.

successive amplifiers, each featuring a gain of G_i and a noise temperature of T_i where i is the index. The Friis formula states that the output temperature is

$$T_{\text{out}} = T_1 + \frac{T_2}{G_1} + \frac{T_3}{G_1 G_2} + \cdots + + \frac{T_{N-1}}{G_1 G_2 \cdots G_N} \tag{2.1}$$

which leads us to conclude that T_1, or the noise added by the first amplifier, is the dominant source of noise for the output of the measurement chain. Thus, the use of a low noise, high gain 'preamplifier' dramatically boosts the efficiency of the entire chain.

2.1 Quantum amplifiers and metrics

Here we discuss the origins of the JTWPA by turning to the concept of parametric amplification, and explore the move toward phase-sensitive cavities, phase-preserving traveling wave devices, and more exotic architectures. An important metric for evaluating such devices is **quantum efficiency**, which is a measure of how much information is recovered at the output of the measurement chain, versus the fundamental quantum limit of how much the measurement chain should be able to preserve [8]. Realistically, the preamplifier should provide a balance of gain level, bandwidth, noise added, and quantum efficiency performance.

2.1.1 Parametric amplification

Parametric amplifiers were first proposed by Cullen et al. as a novel strategy which did not add extra power to the signal tone itself, but instead transferred power from

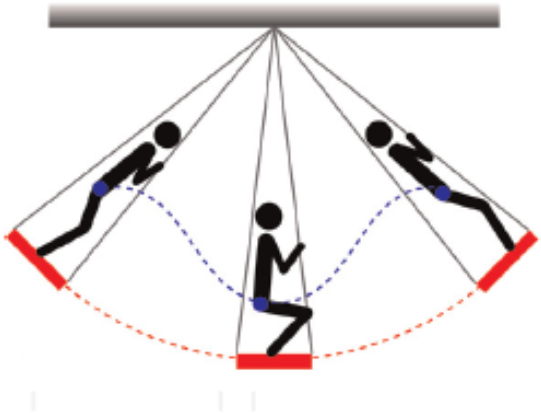

Figure 2-2: Simplified toy model describing the concept of parametric amplification.[2]

a separate pump tone through a nonlinear interaction [37]. In general, this leads to many desirable qualities: parametric amplifiers can be broadband, low-noise, high gain, and easily tunable in terms of frequency. A popular toy model for parametric amplification is that of a "child on a swing", shown in Fig. 2-2. In this figure, the signal tone is the periodic back-and-forth motion of the swing; the pump tone can be understood as a periodic action the child takes to change their center of mass, such as standing up and crouching down, in such a way that amplifies the magnitude of the swinging action itself. We see that the process of amplification transfers energy from this separate action, taken by the child, instead of a direct injection of energy into the swinging motion (such as an external source pushing the swing). Though this model does not exactly capture the nonlinearity needed to induce this interaction in realistic devices, it is suitable for understanding the basic concept of parametric amplification [2].

The qualities of parametric amplification are all desirable for the high-sensitivity experiments described above. As the theoretical background for superconductivity was developed, Brian Josephson discovered the Josephson effect, which became a way to provide nonlinearity for superconducting devices, further explored in section 3.1. Researchers started utilizing this nonlinearity to promote mode interaction (or in the language of optics, wave mixing) processes in thin-film, chip-based devices, described below.

2.1.2 Cavity-based parametric amplifiers

One of the prevalent uses of Josephson non-linearity is a Josephson Parametric Amplifier (JPA) [25, 38, 39, 27, 40, 41, 42]. This device is a parametric oscillator, consisting of a resonator shunted by a Josephson junction or junction array. In operation, the pump and signal tones are sent through a transmission line to which the JPA is coupled, and the JPA will amplify any intra-cavity field that is close to its resonant frequency, which is fundamentally narrowband, although strategies have emerged for improved impedance engineering to widen the bandwidth to 640 MHz [27] and to provide tunable frequency operation to cover a wider total bandwidth, most recently up to 2 - 18 GHz[38, 40].

Since it is possible to control the relative phase relation of the signal and pump, the JPA is also known as a "phase-sensitive" device, with a mode for squeezed operation that enables noise performance to approach and go beyond the noise performance defined by the standard quantum limit [25, 38]. Devices utilizing phase-sensitive amplification include the Josephson Parametric Dimer amplifier, Snail Parametric Amplifiers, the rf-SQUID JPA, and the Field-Programmable JPA, which usually provide full system qubit readout efficiencies of $60\% - 75\%$ for approximately 24 tot 26 dB gain over, a typical bandwidth of around 7-26 MHz [43, 44, 45, 46]. More direct embedding of the qubit with a flux-pumped phase-sensitive JPA results in a measurement efficiency of 80% [47]. In addition, a recent relatively broadband design, the CPW-based broadband impedance-transformed parametric amplifer (CIMPA), leverages a similar integration method to achieve over 20 (15) dB gain over a 200 (700) MHz bandwidth with near quantum-limited added noise, and features a tunable operating frequency [48].

The capability to achieve quantum-limited noise performance in either phase-preserving or phase-sensitive mode makes JPA and JPA-based devices popular candidates for experiments such as qubit readout and axion dark matter searches. For the latter, the HAYSTAC experiment operates a SQUID-based JPA around 5.6 GHz with a fairly narrow bandwidth of 2.3 MHz, as well as a JPA in conjunction with a

squeezed state receiver [49, 25]. Dark matter detection experiments such as QUAX have focused on fully characterizing and developing novel calibration methods for RF amplification chains, utilizing both JPAs and JTWPAs for axion searches around 10 GHz [50, 51, 52]. Thus far, these experiments have operated the JPA in phase-preserving mode and achieved a full system efficiency of approximately $55\% - 59\%$ [51, 53, 52]. We note that the highest full system efficiency currently reported from phase-preserving mode JPAs was measured in a qubit readout experiment and is at 62% [41, 42] relative to an ideal phase-preserving amplifier.

2.1.3 Traveling-wave architecture parametric amplifiers

To overcome narrow instantaneous bandwidth limitations, we consider traveling wave architectures, which utilize Josephson nonlinearity over a long interaction length by chaining many junctions together; this leads to a broad intrinsic bandwidth as the signal no longer has to be exactly resonant with a particular caivity to experience amplification. Early designs performed poorly due to phase-matching limitations [23, 37]. Subsequent realizations of this architecture utilized the high kinetic inductance of NbTiN, with periodic loading structures to maintain phase-matching in a 4 wave-mixing (4WM) regime [54]. Instead of Josephson junctions, the nonlinearity originates from the kinetic inductance in a thin superconducting wires that varies with DC current, where nonlinear scaling is scaled by the critical current of the superconducting material used. These Kinetic Inductance Traveling Wave Parametric Amplifiers (KIT-TWPAs) can be conceptualized as lumped-element LC ladder transmission lines with periodically varying inductance and capacitance values in each unit cell, which opens up a photonic bandgap near the pump harmonics, thus manipulating the dispersion to achieve phase-matching. However, due to the high kinetic inductance in the KIT transmission line, initial designs proved hard to impedance match to 50 Ohm meausurement chains, and the scale of nonlinearity required a long transmission line to achieve $>$ 20 dB gain, as well as relatively high pump power and therefore high dissipation requirements. Newer iterations address these issues by reducing the phase velocity and implementing stop-band engineering

strategies (such as phase-matching resonators from [6] in traditional 4WM KITs [55]), by switching to 3-wave mixing (3WM) regimes to reduce the pump power requirements as in [56], or by utilizing millimeter-wave pump tones to tune the inductance in microstrip geometries for wideband performance [57, 58]. The noise performance of KITs has traditionally been limited by the high power operation requirements, but has recently reached near-quantum-limited levels [59, 57, 58].

However, due to the power handling requirements of KITs, existing impelmentations usually operate at a temperature of 4K, which provides a good balance of minimal noise and power dissipation capability; this operating temperature is not low enough for KITs to act as effective preamplifiers for superconducting qubits in a 20 mK mixing chamber. Thus, the use of Josephson junctions in TWPAs (dubbed JTWPAs) developed in parallel, since they feature stronger nonlinearity per junction and thus require lower pump powers and shorter device lengths to achieve 20 dB of amplification [7]. We take a closer look at phase-matching in JTWPAs: for a device with signal and pump tones, even if we can control the relative phase relation between the tones, this will change throughout the length of a traveling wave devices. Self-phase modulation (where the tone modifies itself) and cross-phase modulation (where the different tones undergo photon-photon interaction) lead to phase mismatches that break the conservation of momentum and energy needed for an efficient wave mixing process [2, 60]. There are several engineering solutions that have been proposed to mitigate these phase mismatches in JTWPAs; in Section 3.3, we explore the canonical example of resonant phase matching in a 4WM device, in which LC resonators are periodically inserted into the transmission line in order to generate a stop band in the dispersion relation and recover phase-matched operation at frequencies near the pump tone [6, 18]. This strategy effectively phase-matches the system around the frequency of the LC resonators and allows JTWPAs to achieve high gain of > 20 dB over several GHz of bandwidth; however, the fabrication requirements for this design, featuring thousands of unit cells and hundreds of LC resonators, are quite difficult to achieve [61].

Alternate strategies have also been proposed, most notably inserting supercon-

ducting quantum interference devices (SQUIDs) that allow nonlinearity tuning with a magnetic field; generally, these designs are less difficult to fabricate, but require additional flux tuning capability [39, 62, 20]. This ability to tune higher-order dispersion nonlinearities enables the use of 3-wave mixing (3WM) regimes, which can lead to even elower pump power and less stringent phase matching requirements [62, 20]. Further exploration of bias tuning by Miano et. al. [63] added inductive SQUIDs (instead of JJs) symmetrically around the transmission line, allowing independent tuning of the both second and third order nonlinearities with a separate bias current, and to a wide bandwidth without the need for a resonant structure. Similarly, Ranzani et al. have designed a reversed Kerr TWPA that achieves phase matching with a sign reversal of third-order nonlinearity, which also results in phase-matching without the need for additional dispersion engineering [21].

These advances established the JTWPAs as a reliably broadband, high-gain device for qubit readout experiments; however, the noise performance of broadband devices remained approximately 20% below ideal noise performance as defined by the standard quantum limit, i.e. quantum efficiencies of approximately 80%. In contrast, the previously discussed cavity-based narrowband JPA amplifiers, operating in phase-preserving or phase-sensitive mode, are capable of reaching or surpassing the ideal noise performance as defined by the quantum limit. Extensive investigation conducted by Peng et.al. led to the realization that information in broadband JTWPAs experienced loss to higher-order sidebands, and that it could be recovered by utilizing adiabatic Floquet physics in device design; the device measured in this thesis follows this scheme, which is further discussed in Section 3.4 [7, 1, 64].

New research on JTWPAs continue to proliferate in recent literature, aiming to directly address the issues of impedance mismatch and isolation in TWPAs. In particular, Chang et. al. utilizes a coplanar waveguide architecture to reduce the insertion loss of a CP-JTWPA to below 1 dB up to 12 GHz, which is similar to the physical platform pursued in this work to reduce insertion loss [31]. Their work utilizes periodic loading for phase-matching, and introduces a window function for the weight of the periodic loading to mitigate the intrinsic ripple; this is a spatial variation of

the periodic loading, not the nonlinearity as in a Floquet TWPA. The CP-JTWPA is able to achieve high, broadband gain over a bandwidth of several GHz, as well as an added photon noise of 0.63 photons, which is closer to quantum-limited than previous experimentally realized JTWPA designs; however, this noise measurement was performed in an idealized impedance environment with attenuators next to the CP-JTWPA [31], which is a configuration not suitable for qubit readout.

Further advances include work demonstrated by Nililson et. al., which features a 3WM TWPA with a deliberately engineered cutoff frequency to prevent up-conversion, a gap in the frequency spectrum to provide phase-matching, and impedance matching networks at both ports of the TWPA; this design provides high gain per unit cell and therefore simplifies and shortens device design [65]. In addition, Gaydamanchenko et. al. pushed the operating bandwidth of 3WM TWPA gain performance to the octave scale, by utilizing periodic variations of the capacitances to ground which allowed for lower dispersion in the signal band, instead of relying on low plasma frequency for phase-matching [22]. Furthermore, Malnou et al. have introduced the TWPAC, which is a TWPA incorporating both forward gain and backward isolation through frequency conversion of backpropagating signals, and they were able to achieve -20 dB isolation without the use of bulky conventional circulators and isolators [66]. In addition, applications such as quantum radar with a JTWPA and a phase-conjugate receiver have been proposed [67]. We note that all these related topics highlight that JTWPA devices can be tailored to a wide range of disciplines, and the suitability of JPAs versus JTWPAs depends heavily on the specific experiment targets of instantaneous bandwidth, gain, quantum efficiency, and dynamic range.

2.2 Power calibration methods

In order to evaluate how these quantum amplifiers perform, we need to obtain a reliable calculation of their respective quantum efficiencies, which depends on a precise calibration of the power of the signal tone, or mean photon number, exactly at the input of the amplifier. Due to cryogenic operation in dilution refrigerators,

determination of this power relies on in situ experiments involving the tools we already have: either matched load noise sources or superconducting qubits. The former 'Y-factor method' relies on sources that produce a known amount of noise, such as a coaxial cable [68, 69] or shot noise tunnel junction [70, 29]; however, these methods both involve intermediate microwave networks between the source itself and the rest of the measurement chain, leading to uncertainties of about 1-2 dB along the line. In this thesis, we focus on qubit-based power calibration methods which provides a measure of quantum efficiency with minimal additional uncertainties.

2.2.1 Qubit dephasing vs. information acquisition rate

A standard method used to evaluate efficiencies follows the definition of quantum efficiency itself, as a measure of how fast a qubit dephases versus how fast we are able to acquire information from this qubit, or Γ_m/Γ_{tot}. This method benefits from the fact that the qubit is already the device under study; thus, measuring its SNR and dephasing performance is convenient for many [71, 44, 45, 47, 18]. Here the SNR is defined as the average separation over the average standard deviation of homodyne voltage histograms from a projective qubit readout, and the dephasing can be determined through a weak measurement inserted into a Ramsey sequence. It is crucial to use strategies such as post selection and active reset to ensure that the qubit states initialized and measured are in relatively pure states, so the any errors present are fundamentally due to the nature of the measurement chain, instead of other decoherence effects. Various different strategies may be used here, including integration over readout time [18] or the resonator drive strength [71, 44, 45]. Generally, these results focus on the full system efficiency of the measurement chain instead of the individual components, since that is what matters for effective qubit readout. Representative numbers from recent literature range from approximately $16.5 \pm 2\%$ for a relatively lossy niobium uniform JTWPA measurement chain [71], to $72.4 \pm 4\%$ for the field programmable phase-sensitive (FPJA) device [45], and 80% for a combined on-chip JPA, JPA, and JTWPA measurement chain [47].

2.2.2 Qubit dephasing and the AC stark shift

In order to obtain a more precise power calibration, researchers have also explored the relationship between the qubit dephasing, AC stark shift, and the resonator drive power incident on the qubit. In this method, we independently measure the cavity frequency ω_r and output coupling rate κ_c to calculate $P = \kappa_c \hbar \omega_r \overline{n}$ [72, 18]. First, similar to the qubit characterization experiments outlined above, κ and ω_r are found with Lorentzian fits to the resonator transmission. Then, cross-verification of χ and κ can be done with fits to dephasing and the AC stark shift vs versus a weak measurement-induced dephasing experiment. After ascertaining the incident power, a simple noise rise experiment can give the SNR improvement provided by the device and measurement chain under study, from which we can extract the noise temperature of the full system, as well as individual devices, conditional on knowledge of insertion loss between components in the system. This method is reliable and involves multiple cross-checks, though it is limited by its narrowband nature; since the measurement is frequency dependent, the only reliable power calibration result is near the resonator frequency. We explore this method, denoted as the “cQED dephasing method", further in Chapter 6.

2.2.3 Waveguide QED: qubit coupled to open transmission line

To obtain a more broadband power calibration, which is suitable for devices like the JTWPA, we turn to another qubit configuration that utilizes the strategy of waveguide quantum electrodynamics, or wQED. This method features a qubit coupled to an open transmission line, which can act as a perfect reflector at low input power, and a perfect transmitter at high input power; fitting its transmission behavior allows us to extract the exact power at the qubit [29, 73]. Since the qubit is operated in transmission, there is no need for additional bulky and lossy circulators, and we can situate the qubit in parallel with any amplifier under study, thereby eliminating the need for precise knowledge of the insertion loss between the calibration device and

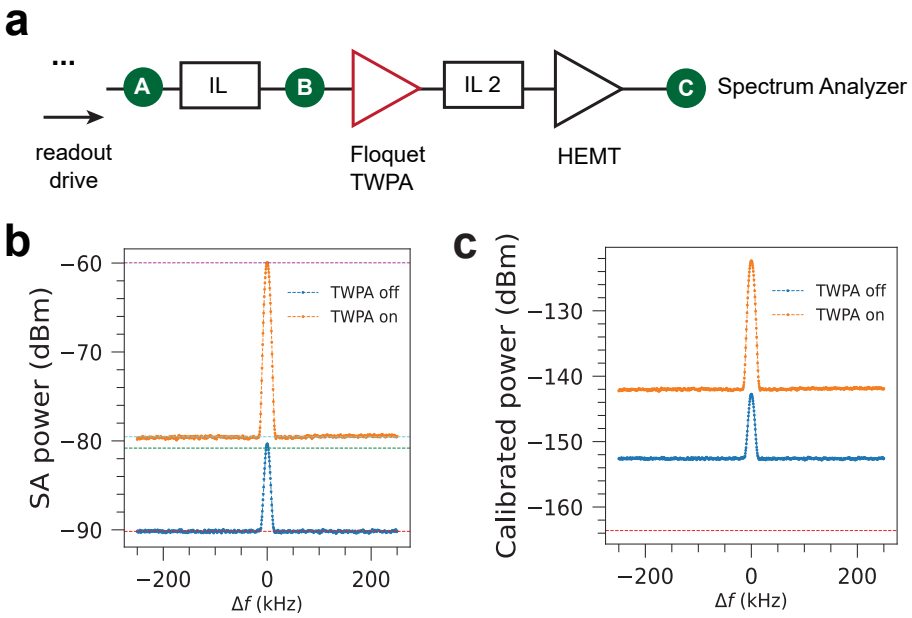

Figure 2-3: (a) Simplified measurement chain with which to derive quantum efficiency if we know the power at reference plane **A**, obtained from the circuit QED power calibration, or reference plane **B**, obtained from the waveguide QED power calibration. For the former, we also need to know the insertion loss between **A** and **B**, which we estimate from a dunk test. The second insertion loss between the TWPA and the HEMT not necessarily directly measured or calculated, but included in the overall system efficiency. (b) Measured signal with the TWPA on (orange line) and off (blue line). We fit both curves with a gaussian to extract the respective signal and noise (dark blue, green dashed lines). (c) After obtaining the power calibration, we find a fixed difference factor, defined as the difference between the signal while TWPA pump is off, and the calibrated power while TWPA is off. We can then replot our curves with respect to the standard quantum limit. Here we use the results from the cQED calibration, but the process is exactly the same for the wQED calibration.

amplifier. Since the qubits can be flux tunable, this calibration can also be broadband; we explore the implementation and implications of this strategy in Chapter 5.

2.3 Quantum efficiency derivation

Generally, once we obtain an absolute power reference at the input of an amplifier, we can perform noise measurements with the amplifier turned on and off to extract the system and intrinsic quantum efficiency. Consider the simplified readout chain diagram shown in Figure 2-3(a), in which we combine and abstract various cir-

cuit components to several functional blocks, without loss of generality: the Floquet TWPA and HEMT amplifiers, each with added noise and gain, as well as insertion loss before and between the amplifiers. We define reference planes **A**-**C** for clarity. From the cQED calibration with a qubit operated in reflection, we can obtain the absolute power value at plane **A**, while from the wQED calibration with a device situated in parallel, we can obtain the absolute power value at plane **B**; the full process for these calibrations is provided in Chapters 5 and 6. The insertion loss between these points can be estimated from a dunk test of the components (cables, circulator, and directional coupler) in liquid nitrogen. We will use the following notation: S_X and N_X refer to the calibrated power of the signal and noise floor at the reference plane **X**, and additional subscripts $_{\text{amp,i}}$, and $_{\text{sys,on(off)}}$ denote values concerning the intrinsic performance of the TWPA itself and full system performance while the TWPA is on (off), respectively. For instance, $S_{A,\text{sys,off}}$ corresponds to the signal power at reference point **A** while the TWPA is turned off.

From the room temperature measurements at **C** and power calibration at **A**, we extract the system gain, downstream gain (when TWPA is turned off), and amplifier gain in linear scale:

$$\begin{aligned} G_{\text{sys,on}} &= S_{D,\text{sys,on}}/S_{A,\text{sys,on}} \\ G_{\text{sys,off}} &= S_{D,\text{sys,off}}/S_{A,\text{sys,off}} \\ G_{\text{amp,i}} &= S_{D,\text{sys,on}}/S_{D,\text{sys,off}}. \end{aligned} \tag{2.2}$$

From the gain values, we can then extract the noise temperature from noise power by dividing by the Boltzmann constant k_B and the resolution bandwidth $B = 10\,\text{kHz}$ on the spectrum analyzer:

$$T_{\text{sys,on(off)}} = \frac{N_{A,\text{sys,on(off)}}}{k_B B} = \frac{N_{D,\text{sys,on(off)}}/G_{\text{sys,on(off)}}}{k_B B}. \tag{2.3}$$

The system measurement efficiencies with the TWPA on and off can thus be calculated from the noise temperatures using Equation (5.3), repeated here for convenience.

$$\eta_{\text{sys,on(off)}} = \frac{\hbar\omega}{k_B T_{\text{sys,on(off)}}} \tag{2.4}$$

Finally, we calculate the amplifier intrinsic quantum efficiency from the extracted system noise metrics. The total noise photon numbers when the TWPA is turned on and off (including the 1/2 vacuum noise photon) referred at the amplifier input are

$$n_{\mathrm{sys,on(off)}} = \frac{k_B T_{\mathrm{sys,on(off)}}}{\hbar\omega} = 1/\eta_{\mathrm{sys,on(off)}}, \tag{2.5}$$

and the added noise photon number from the Floquet TWPA is thus

$$A_{\mathrm{amp,i}} = (n_{\mathrm{sys,on}} - 1/2) - \left(\frac{n_{\mathrm{sys,off}} - 1/2}{G_{\mathrm{amp,i}}}\right), \tag{2.6}$$

resulting in the normalized intrinsic efficiency [7]

$$\begin{aligned} \tilde{\eta}_{\mathrm{amp,i}} &= (1 + 2A_{\mathrm{amp,i}})^{-1}/\eta_{\mathrm{ideal}}(G_{\mathrm{amp,i}}) \\ &= \frac{2 - 1/G_{\mathrm{amp,i}}}{1 + 2A_{\mathrm{amp,i}}} \\ &= \left(\frac{2}{\eta_{\mathrm{sys,on}}} - \frac{2}{G\eta_{\mathrm{sys,off}}} + \frac{1}{G}\right)^{-1} \Big/ \eta_{\mathrm{ideal}}(G). \end{aligned} \tag{2.7}$$

Chapter 3

Building a JTWPA

3.1 Circuit Quantum Electrodynamics

3.1.1 Josephson Junctions

The phenomenon of superconductivity involves cooling a material down beyond a critical temperature, which results in a 'supercurrent' that can flow without dissipation in the material. In a microscopic model of superconductivity, known as Bardeen–Cooper–Schrieffer (BCS) theory, this supercurrent can be explained by the pairing of electrons into 'Cooper pairs', which result from a slight attraction between the electrons due to coupling with lattice vibrations at low temperatures. Since these electron pairs exhibit boson-like behaviors and stay paired together, electron flow does not experience any resistance [3]. This is desirable for a number of applications, including dissipationless electronics and superconducting quantum computing.

In particular, Brian D. Josephson discovered in 1962 that supercurrents could tunnel between a thin layer of dielectric sandwiched between two superconducting metals [74]. Deemed the Josephson effect, this phenomenon occurs even without a voltage potential difference. In addition, when there is a voltage drop, the supercurrent will oscillate at a frequency that is proportional to the voltage drop and dependent on the magnetic environment. The physical junction itself is called the Josephson junction (JJ), which has the typical structure shown in Fig. 3-1.

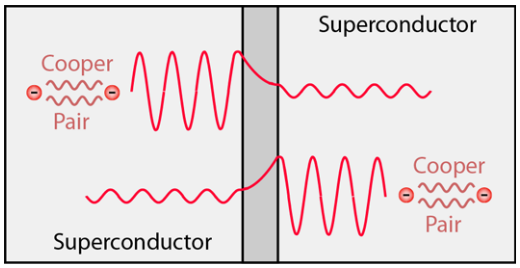

Figure 3-1: **Typical Josephson junction schematic.** Coupled electron Cooper pairs, drawn in red, tunnel from the superconducting layers (light gray) across a thin insulating layer (dark gray), with exponential decay and oscillatory behavior akin to that of free particle wavefunctions.[3]

As shown in the figure, the two superconducting layers are separated by a thin insulating layer, and Cooper pairs on either side of the junction can tunnel through the insulating barrier. The wavefunctions of these paired electrons resemble free electron tunneling behavior, showing exponential decay upon tunneling. This effect can be illustrated with the constitutive relations of Josephson junctions, which delineate the dependence of current and voltage on phase, shown in Eq. 3.1.

$$I = I_0 \sin \varphi V = \frac{\Phi_0}{2\pi} \frac{d\varphi}{dt} \tag{3.1}$$

In Eq. 3.1, the junction parameter I_0 is the critical current of a Josephson junction and ϕ is the gauge-invariant phase difference across the junction. In Eq. 3.1, the constant term $\frac{\Phi_0}{2\pi} = \frac{\hbar}{2e}$ is the reduced flux quantum. Taken together, these equations result in the nonlinear JJ inductance in Eq. 3.2, namely

$$L_J = V(t) / \left(\frac{\mathrm{d}I(t)}{\mathrm{d}t} \right) = \frac{\Phi_0}{2\pi I_0 \cos(\phi)}. \tag{3.2}$$

From this equation, we see that the inductance of the Josephson junction is non-linear, which will be crucial for application in JTWPAs and various other quantum devices.

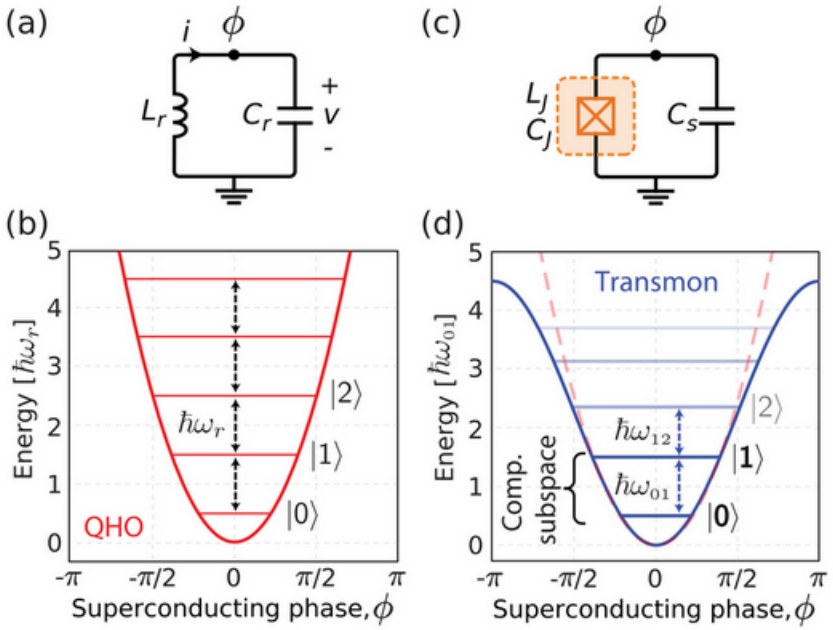

Figure 3-2: Comparison of quantum oscillators by Krantz et al [4]: (a) Circuit schematic of a standard LC resonator, which serves as a convenient analog for the quantum harmonic oscillator. (b) Energy levels of a quantum harmonic oscillator are equally spaced. (c) Circuit schematic of an LC resonator, in which the inductor is replaced with a Josephson junction that is subject to the constitutive relation of dependence of current and voltage on phase. (d) Energy levels of an anharmonic quantum harmonic oscillator are not equally spaced, modelling the behavior of the circuit in (c).

3.1.2 The Quantum LC oscillator

To build a realistic device, we first consider the classical description of an LC resonator, then incorporate nonlinearity with Josephson junctions. A classical LC resonator consists of an inductive (L_r) and capacitive (C_r) component in parallel, where the energy oscillates between magnetic and electric forms, see Fig. 3-2(a). In the classical Hamiltonian formation, we can draw an analogy between an LC circuit and masses on springs, where the kinetic energy corresponds to the electrical energy, and potential energy corresponds magnetic energy. We can write the Hamiltonian in the generalized circuit coordinates of flux and charge, which we define from their rela-

tionship with voltage and current:

$$\begin{aligned} \Phi(t) &\equiv \int_{-\infty}^{t} V\left(t'\right) dt' \\ Q(t) &\equiv \int_{-\infty}^{t} I\left(t'\right) dt' \end{aligned} \tag{3.3}$$

Using charge Q as the conjugate coordinate, we therefore write the Hamiltonian in a form closely resembling a harmonic oscillator,

$$H(\Phi, Q) = Q\dot{\Phi} - \mathcal{L} = \frac{Q^2}{2C} + \frac{\Phi^2}{2L}. \tag{3.4}$$

By convention we can define the reduced flux $\hat{\varphi} \equiv 2\pi\hat{\Phi}/\Phi_0$ and reduced charge $\hat{n} \equiv \hat{Q}/2e$ to rewrite the Hamiltonian into

$$\hat{H}_{LC} = 4\frac{e^2}{2C}\hat{n}^2 + \left(\frac{\Phi_0}{2\pi}\right)^2 \frac{\hat{\varphi}^2}{2L}. \tag{3.5}$$

To convert this description into a quantum harmonic oscillator (QHO), we impose the commutation relation $[\hat{\Phi}, \hat{Q}] = i\hbar$ for these conjugate variables in Eq. (3.5), and we also factor the Hamiltonian in the typical quantum harmonic oscillator form $\hat{x}^2 + \hat{y}^2 = (\hat{x} + i\hat{y})(\hat{x} - i\hat{y}) - i[\hat{x}, \hat{y}]$. Then we obtain

$$\hat{H} = \left(\frac{\hat{\Phi}}{\sqrt{2L}} + i\frac{\hat{Q}}{\sqrt{2C}}\right)\left(\frac{\hat{\Phi}}{\sqrt{2L}} - i\frac{\hat{Q}}{\sqrt{2C}}\right) - \frac{i}{2\sqrt{LC}}[\hat{Q}, \hat{\Phi}] \tag{3.6}$$

which can be defined by a single operator

$$\hat{a} = \frac{1}{\sqrt{\hbar\omega}}\left(\frac{\hat{\Phi}}{\sqrt{2L}} - i\frac{\hat{Q}}{\sqrt{2C}}\right) \tag{3.7}$$

and thus rewritten into the form of a quantum harmonic oscillator,

$$\hat{H} = \hbar\omega\left(\hat{a}^\dagger\hat{a} + \frac{1}{2}\right) \tag{3.8}$$

.

This resonator will have the form shown in Fig. 3-2(b) of a harmonic oscillator,

hosting states with a fixed energy spacing of $\hbar\omega$.

However, if we want a system that will work for a superconducting device such as a qubit, we will need to distinguish and excite the oscillator states with fine-grained control; if the energy spacings are equal, we cannot reliably transition between the ground and first excited state only. Therefore, we add nonlinearity to the harmonic oscillator by incorporating a Jospheson junction instead of a linear inductor, as shown in Fig. 3-2(c). Recall that the expression in Eq. (3.3) for the inductance of the Josephson junction can be brought into the Hamiltonian of Eq. (3.6), giving us the anharmonic Hamiltonian

$$\hat{H}_{an} = 4\frac{e^2}{2C}\hat{n}^2 - \frac{\Phi_0}{2\pi}I_0\cos(\hat{\varphi}). \tag{3.9}$$

This quantized circuit features unequal energy spacings between state transitions, such as the $\hbar\omega_{01}$ and $\hbar\omega_{12}$ called out in Fig. 3-2(d). Adding the Josphsen junction allows this circuit to function as an 'artificial atom' that can be customized, driven, and measured in a wide range of quantum computing and sensing experiments.

3.2 The nonlinear wave equation

In this section, we explore the theory and design of the standard JTWPA device. We consider a LC ladder transmission line with capacitively shunted Josephson junctions, as shown in Fig. 3-3. From this figure, we see that instead of a linear inductor in the LC resonators of each unit cell in the ladder, we have used a Josephson junction instead, adding the same desirable nonlinearity in that of the quantum anharmonic oscillator, which in this case encourages the interaction between a signal and pump tone.

Within a transmission line with short spacing between each unit cell, we can engineer the nonlinear effect from the Josephson inductance to dominate over the linear inductance of the transmission line itself. For simplicity, we assume the ground capacitors all have the same value, $C_n = C_0$, and we continue to assign L_J to be the

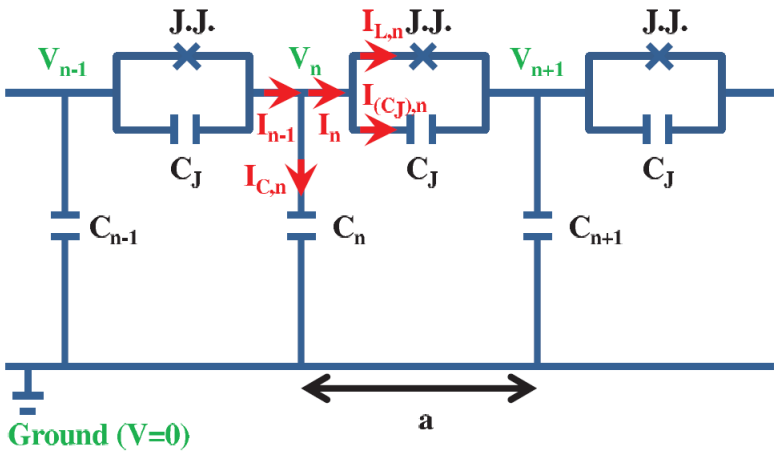

Figure 3-3: **Typical JTWPA schematic.**[5] JJs are represented by a cross in the circuit schematic, and are located in a resonator configuration with a capacitor C_J; this is analogous to the LC resonator, though the JJs are nonlinear. Each unit cell is spaced a distance a apart, and denoted by number n. Thus, we can see that there are capacitors to ground for each unit cell labeled C_n and so forth. The current and voltage in each unit cell are also represented by I_n and V_n, where a subscript of $I_{C,n}$ indicates current along the branch of the shunt capacitor.

nonlinear Josephson inductance. Then we index each unit cell with a number n and can thus write equations for Kirchoff's laws, the capacitor current-voltage relation, and the Josephson current relation. By using a continuum approximation, we can obtain and solve the nonlinear wave equation for this system. This derivation is detailed in Yakkobi, et al.[5] and the supplement of O'Brien, et al. [6] ; here we go directly to the result in Eq. 3.10.

$$C_0\frac{\partial^2\phi}{\partial t^2} - \frac{a^2}{L_J}\frac{\partial^2\phi}{\partial x^2} - C_J a^2\frac{\partial^4\phi}{\partial x^2\partial t^2} = \frac{a^4}{2I_0^2L_J^3}\frac{\partial^2\phi}{\partial x^2}\left(\frac{\partial\phi}{\partial x}\right)^2 \tag{3.10}$$

In this equation, the terms on the left hand side are the weakly dispersive linear waves, which have phase velocity that depends on spatial and temporal parameters, while the term on the right hand side describes the cubic nonlinearity of the system. Note that we are using the follwing ansatz solution in Eq. 3.11, which is a superposition of the pump, signal and idler waves, where A_m is the amplitude of each wave under the slowly varying envelope approximation (SVEA) [6].

$$\phi = \frac{1}{2}\left[A_p(x)e^{i(k_p x+\omega_p t)} + A_s(x)e^{i(k_s x+\omega_s t)} + A_i(x)e^{i(k_i x+\omega_i t)} + c.c\right] \tag{3.11}$$

Following the typical SVEA assumptions, neglecting higher order dependencies, and separating out pump, signal and idler terms, we obtain the coupled wave equations for the system shown below

$$\begin{aligned} A_p(x) &= A_{p,0}e^{i\alpha_p x} \\ \tfrac{\partial A_s}{\partial x} - i\alpha_s A_s - i\kappa_s A_i^* e^{i(\Delta k_L+2\alpha_p)x} &= 0 \\ \tfrac{\partial A_i}{\partial x} - i\alpha_i A_i - i\kappa_i A_s^* e^{i(\Delta k_L+2\alpha_p)x} &= 0 \end{aligned} \tag{3.12}$$

where the indexed self- and cross-phase modulation coefficients α, as well as coupling coefficients κ, are defined separately for signal, idler, and pump as follows.

$$\begin{aligned} \alpha_s &= \tfrac{2\kappa k_s^3 a^2}{L_J C_0 \omega_s^2} & \kappa_s &= \tfrac{\kappa(2k_p-k_i)k_s k_i a^2}{L_J C_0 \omega_s^2} \\ \alpha_i &= \tfrac{2\kappa k_i^3 a^2}{L_J C_0 \omega_i^2} & \kappa_i &= \tfrac{\kappa(2k_p-k_s)k_s k_i a^2}{L_J C_0 \omega_i^2} \\ \alpha_p &= \tfrac{\kappa k_p^3 a^2}{L_J C_0 \omega_p^2} & \kappa &= \tfrac{a^2 k_p^2 A_{p,0} A_{p,0}^*}{16 I_0^2 L_J^2} \end{aligned} \tag{3.13}$$

These equations are analogous to the case of an optical parametric amplifier operating in a four-wave mixing regime, which also has coupled wave equations for the pump, signal, and idler using the strong pump approximation [6]. Extending this analogy, we can obtain solutions to Eqs. 3.12. For example, the signal amplitude at position x is given by Eq. 3.14:

$$A_s(x) = \left[A_s(0)\left(\cosh gx - \frac{i\Delta k}{2g}\sinh gx\right) + \frac{i\kappa_s}{g}A_i^*(0)\sinh gx\right]e^{i\Delta k x/2} \tag{3.14}$$

where the gain coefficient is defined as

$$g = \sqrt{\kappa_s \kappa_i^* - (\Delta k/2)^2} \tag{3.15}$$

and the phase matching parameter has become

$$\Delta k = \Delta k_L + 2\alpha_p - \alpha_s - \alpha_i = 2k_p - k_s - k_i + 2\alpha_p - \alpha_s - \alpha_i \tag{3.16}$$

From Eq. 3.15, we can note that the gain will depend on how properly phase-matched the system is. If Δk is far away from zero, the signal will experience oscillatory gain that scales only quadratically with device length, while if $\Delta k = 0$, then the signal will depend exponentially on the gain coefficient g and device length, thus achieving significant amplification as desired [6]. This traveling wave architecture is different from that of a traditional cavity amplifier, which only amplifies a narrow band of frequencies around the cavity resonance. In contrast, the JTWPA supports higher gain over a broad frequency band, by utilizing longer device lengths and deep sub-wavelength resonators for phase-matching [6]. Crucially, by tuning the values of the classical inductors and capacitors in each unit cell, we propose to tailor the frequency bandwidth and dynamic range of operation to suit different experimental requirements.

3.3 Phase matching and limitations

Having set up the physical configuration of a JTWPA and motivated the need for proper phase-matching, we now look to engineering solutions to resolve this issue. The canonical example is resonant phase matching (RPM) by O'Brien et al. in 2014, in which the transmission line is not only shunted by ground capacitors, but also periodically shunted by LC resonators with inherent resonant frequency slightly above the pump frequency [6]. This opens up a stop band in the dispersion relation, and by tuning the pump wave vector along the dispersion curve to rephase with the signal tone, phase matching can be achieved [2]. The schematic of this JTWPA design is shown below in Fig. 3-4, adapted from O'Brien et al. Here we observe that the LC resonators are added to each standard unit cell, parallel to the shunted ground capacitor branch. Further dynamical control is achieved by adding a coupling capacitor, C_c, into the shunted branch with the LC resonator. Thus, when the weak signal and strong pump enter the device through the input, they interact with a

medium that has resonant features slightly above the pump tone; this opens up a stop band in the dispersion relationship, as shown in part c).

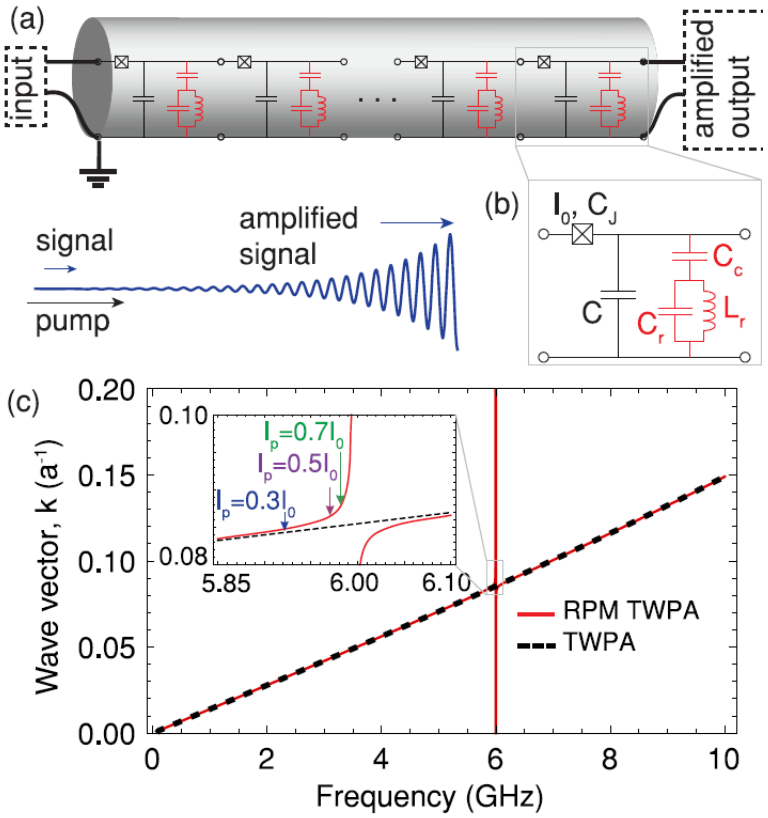

Figure 3-4: **JTWPA with resonant phase matching.**[6] a) The standard JTWPA is modified by adding an LC resonator and coupling capacitor C_c, shown in red, for each unit cell. The amplified signal is indicated by the blue oscillatory curve. b) Inset showing a single unit cell of the JWTPA with resonant phase matching. Note that the convention followed here uses C for the capacitor to ground, instead of C_0 as we have been using. c) The addition of the LC resonator opens up a stop band in the normally linear TWPA dispersion (black dashed line), to result in the RPM TWPA dispersion relation (red solid line). To achieve proper phase matching, we can adjust the pump frequency for different levels of pump current, shown here as $I_p = 0.3I_0$, $0.5I_0$, or $0.7I_0$, until the phase matching parameter $\Delta k = 0$.

We note that we can make the following approximation, in which we neglect dispersion and impedances dependent on frequency. Having done so, the phase-matching expression becomes

$$\Delta k \approx 2k_p - k_s - k_i - 2k_p\kappa \tag{3.17}$$

where $\kappa = \left(a^2 k_p^2 \left|Z_{\text{char}}\right|^2 / 16 L_J^2 \omega_p^2\right) \left(I_p / I_0\right)^2$, and the characteristic impedance of the transmission line is $Z_{\text{char}} \approx \sqrt{L/\left(C_0 + C_c\right)} \approx 50\Omega$. This characteristic impedance is chosen for convenient integration with standard radio- and microwave-frequency electrical components, and places some limits on the choice of circuit parameters. As shown in Eq. 3.17, the phase mismatch can then be adjusted simply by adjusting the pump wavevector k_p. We refer back to Fig. 3-4 c) to better conceptualize the situation. Technically, in the weak pump limit, a standard, linear TWPA dispersion (shown in the black dashed lines) would be perfectly phase matched for a degenerate four-wave mixing process; i.e. the degenerate pump wavevector can be exactly the average of signal and idler wavevectors. However, as we are operating in the strong pump regime, self- and cross-phase modulation result in phase variation as the signal and pump propagate throughout the device. Consequently, we can modify the pump wavevector along the RPM TWPA dispersion relationship, shown in the red solid curved line. The authors have calculated the pump power necessary to phase-match currents of magnitude $I_p = 0.3I_0$, $0.5I_0$, or $0.7I_0$, demonstrating that a dynamic tuning range for an RPM TWPA is practically achievable. Having done so, the authors calculate the exponential increase in gain, and simulate the system to show that the TWPA gain is vastly improved to around 20 dB over a 4 GHz bandwidth, compared to 10 dB over a narrower 1 GHz bandwidth for a non-RPM TWPA. The results are shown in Fig. 3-5. The RPM TWPA, shown in purple, achieves significantly higher and broadband gain, though it has a narrow dispersion feature at the center frequency, due to the existence of a stop band opened by the LC resonators. Furthermore, we note that the phase matching parameter in part b) for an RPM TWPA can be nearly zero close to the center frequency, implying near-perfect phase matching in that operational region.

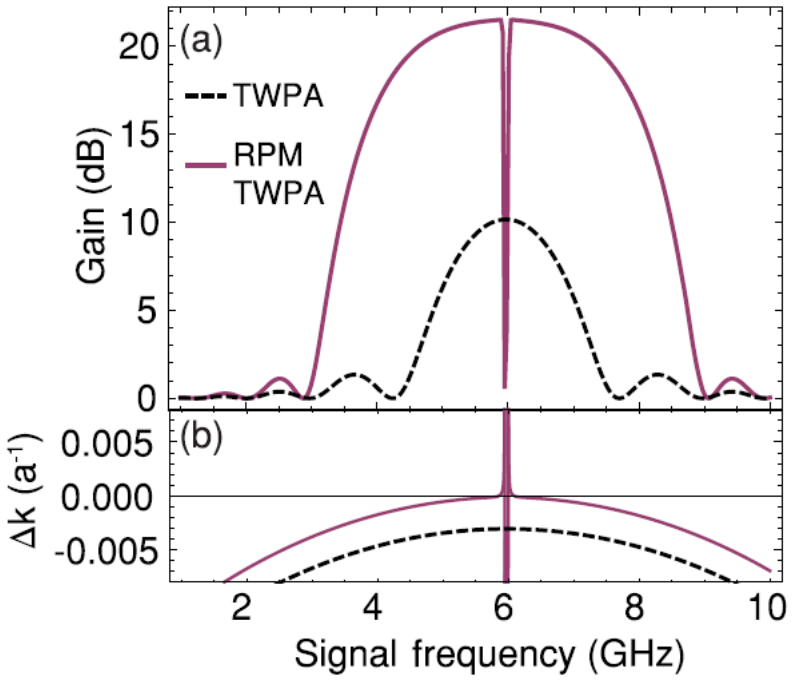

Figure 3-5: **Gain comparison for RPM.**[6] a) The RPM TWPA (purple solid line) and standard TWPA (black dashed line) are modeled with the same pump current and frequency; the only difference is the presence of phase matching resonators in the RPM TWPA. The gain is around 20 dB over a bandwidth of 4 GHz. Note that due to the creation of a stop band, the RPM TWPA has a dispersion feature in the form of a dip around its center frequency, 5.97 GHz. b) The phase matching parameter is shown for a standard and RPM TWPA; we see that the RPM TWPA can achieve near-perfect phase-matching near the center frequency due to tuning of the pump wavevector.

3.4 Mitigating sideband loss with Floquet-mode design

However, even with phase-matching strategies, conventional JTWPA designs still demonstrated noise performance that was about 20% below that of the quantum limit [18, 6]. More extensive modeling completed by Peng et al. considered additional modes of the system, in addition to just the pump, signal, idler etc.; this lead to the understanding that much of the information in the JTWPA was lost due to sidebands [7]. We can conceptualize this by envisioning the profile of JTWPA, relative to an idealized vacuum environment it is situated in. Though we can optimize for

impedance matching, there is still a sharp transition between the vacuum and nonlinear interaction region; therefore, there is a mode mismatch between the input tones and the Floquet modes of the JTWPA, leading to significant sidebands, as shown in Fig. 3-6(e, g, i).

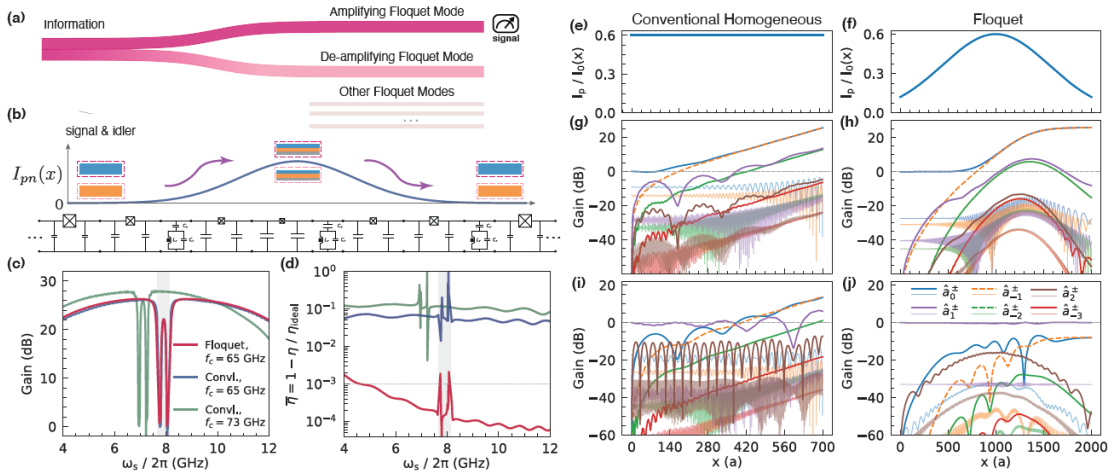

Figure 3-6: **Floquet JTWPA versus uniform JTWPA design.**[7] a) The information in a Floquet TWPA consists of two main modes, an amplifying and deamplifying modes. A uniform TWPA would feature a mixture of these and other higher order modes. (b) The circuit parameters in a Floquet JTWPA are smoothly varied over the length of the device. (c) Theoretical gain curve comparison between convention (uniform) or Floquet JTWPA, showing that the Floquet JTWPA has a wide bandwidth with the same circuit parameters, and it is still able to reach 20 dB gain over a few GHz of bandwidth. (d) Due to recovering losses from sidebands, the quantum efficiency of a Floquet JTWPA is two orders of magnitude closer to that of an ideal amplifier. (e, f) Pump profile of a conventional uniform JTWPA versus a Floquet JTWPA. (g, h) Internal field profiles of the uniform and Floquet JTWPAs for an injected signal mode. (i, j) Internal field profiles of the uniform and Floquet JTWPAs for an injected sideband mode, assuming zero dielectric loss.

The key to recovering these sideband losses is a slow, adiabatic modulation of the input modes, such that they are transformed into Floquet modes inside of the JTWPA and then back into output modes at the end of the device; practically, this involves tapering of circuit parameters at the boundaries of the device. This leads to information recovery in the Floquet mode JTWPA, shown abstractly in Fig. 3-6(a) and more concretely in the reduction of sidebands in Fig. 3-6(h, j). The device under study in this thesis implements a modified Gaussian profile for elements across the

length of a few thousand unit cells, depicted in Fig. 3-6(b, f). This device features improved gain and quantum efficiency performance compared to the uniform JTWPA design, as shown in Fig. 3-6(c), and is further described in Chapter 5, section 5.1. Note that we define the quantum inefficiency in Fig. 3-6(d) as the difference from that of an ideal amplifier, i.e.

$$\overline{\eta} = 1 - \frac{\eta}{\eta_{ideal}}. \tag{3.18}$$

Chapter 4

Floquet TWPA performance metrics

4.1 Device design

The Floquet TWPA is fabricated on a 200-mm high-resistivity ($> 10\,\mathrm{k\Omega{\cdot}cm}$) float-zone silicon wafer using a standard superconducting qubit process [75, 76, 77, 78, 79, 80], consisting of an aluminum ground plane, Josephson junctions [81], and aluminum air bridges [82] as shown in Fig. 4-1(a). Meandered with a 5×40 mm chip footprint, the Floquet TWPA consists of 3008 sets of three-Josephson-junction chains interleaved by open-ended coplanar waveguide stubs, which function as low-loss distributed capacitors to ground. Capacitively coupled lumped-LC resonators centered at ~ 8 GHz are inserted every 8 unit cells to phase-match the desired four-wave-mixing parametric amplification process [6]. The lengths of the Josephson junctions and the coplanar stubs in each cell are jointly varied across the device to control the instantaneous nonlinearity and implement the adiabatic Floquet scheme [7] while maintaining $\sim 50\,\Omega$ impedance matching between cells. The resulting junction critical currents range from $4.62\,\mu$A in the middle to $13.1\,\mu$A at the ends, chosen to balance Floquet mode matching at the interfaces and $\sim -100\,\mathrm{dBm}$ $\mathrm{P_{1dB}}$ gain compression for multiplexing tens of qubits.

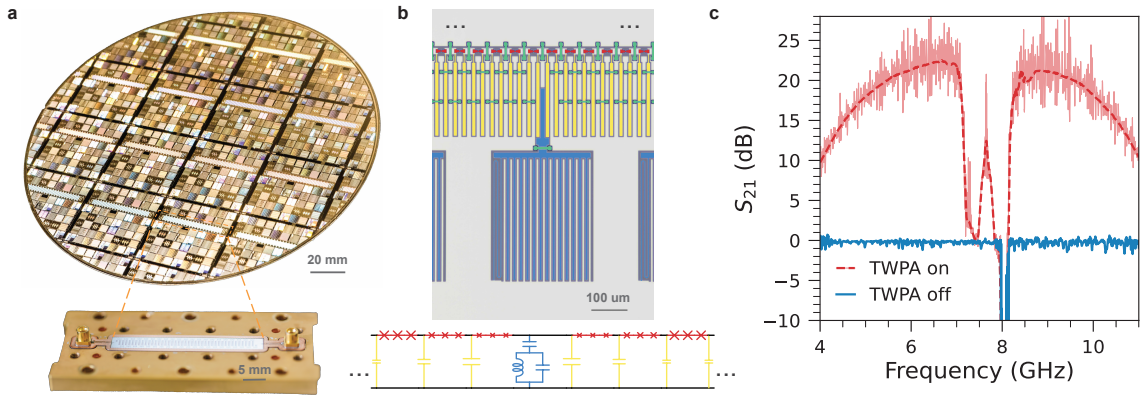

Figure 4-1: (a) Floquet TWPAs are fabricated on a 200-mm silicon wafer using a standard superconducting qubit process. The Floquet TWPA chips are 5×40 mm in size and are housed in a gold-plated package with SMPM connectors. (b) False-color micrograph and circuit schematic of the Floquet TWPA. Each LC ladder of the nonlinear transmission line consists of three Dolan-style Josephson junctions chained in series (red) and a coplanar stub capacitor (yellow) to ground (light gray). The junction sizes and coplanar stub lengths are varied as a function of position across the device. The capacitively coupled phase matching resonators (blue) are inserted every eight unit cells to phase match the parametric amplification process. The airbridges (green) are placed in every cell to connect the grounds on both sides of the junction chains.(c) Measured insertion loss (blue) and broadband parametric gain (light red) of the Floquet TWPA, both normalized to a through line with matching cable lengths in a microwave switch bank; the measurement setup is depicted in Figure 4-1(a). The red dashed line is the parametric gain data smoothed with a Savitzky-Golay filter.

4.2 Gain and insertion loss

As shown in Fig. 4-1(c), The total device insertion loss averages $< 0.5\,\mathrm{dB}$ within the full 4-12 GHz band. Because dielectric loss $A_{\mathrm{dielectric}}[dB] \propto k(\omega)\tan\delta \propto \omega$ is linearly proportional to wavevector $k(\omega)$ and signal frequency ω on the dB scale and our device exhibits a near-zero slope, we attribute the remaining $\sim 0.11\,\mathrm{dB}$ frequency-independent insertion loss to microwave packaging and impedance mismatch, which can be optimized. In addition to minimal insertion loss, our Floquet TWPA exhibits $> 20\,\mathrm{dB}$ parametric gain over an instantaneous bandwidth of $3\,\mathrm{GHz}$ as shown in Fig. 4-1(c). We highlight that the parametric gain reported here in Fig. 4-1(c) is relative to a through line and not to the undriven case. The device is measured in a realistic measurement environment with directional couplers, circulators, and no attenuators which would otherwise improve impedance matching conditions and gain

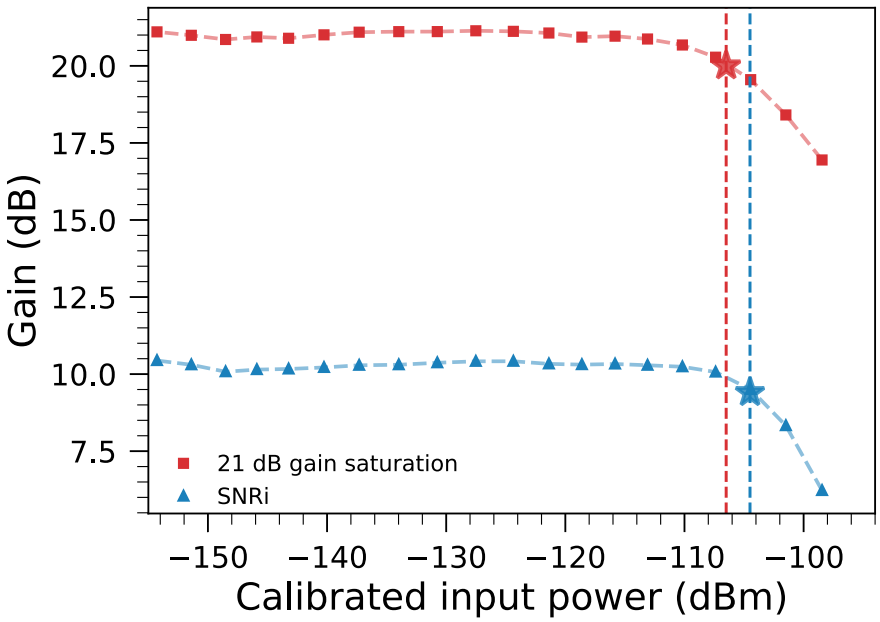

Figure 4-2: Dynamic range of the Floquet JTWPA at a signal frequency of 6.59 GHz shows P_{1dB} at $-106.5\,\mathrm{dBm}$ (red star). The 1-dB SNRi compression point is at $\sim -104\,\mathrm{dBm}$ (blue star), which is 2.5 dB higher than the gain compression point, indicating that the Floquet TWPA achieves improved noise performance compared to conventional counterparts.

performance for TWPAs.

4.3 P1dB and dynamic range

In Figure 4-2, we plot the measured parametric gain and SNRi at 6.59 GHz as a function of the calibrated input signal power. At 21-dB gain, the 1-dB compression point is $P_{\mathrm{1dB}} = -106.5\,\mathrm{dBm}$, as indicated by the red star marker. Remarkably, if we similarly define a 1-dB SNRi compression point as the signal power at which the SNRi lowers by 1 dB from the small-signal-power limit, the 1-dB SNRi compression point occurs at a signal power 2.5 dB higher than the P_{1dB} gain compression point, as indicated by the blue star marker in Figure 4-2. This is in stark contrast to conventional TWPAs, for which the SNRi compression occurs before the signal power reaches the gain compression point [33]. The improved noise performance at high signal power yields another advantage over conventional TWPAs, potentially attributed

to its efficient sideband leakage suppression [30].

The measured $-106.5\,\mathrm{dBm}$ gain compression is on par with those of the experimentally realized conventional JTWPAs ($-110\,\mathrm{dBm}$ to $-95\,\mathrm{dBm}$) reported in literature [18, 20, 29, 21, 83], showing promise for broadband photon emission detection and multiplexed qubit readout applications [84, 33, 85]. Nonetheless, we note that there is still room for improvement of P_{1dB}. The predicted gain compression point, calculated using the pump depletion model [86] indicates a P_{1dB} value $\sim 5.5\,\mathrm{dB}$ higher than the measured value. We hypothesize that the cause for the lower measured P_{1dB} is not signal sideband leakage as in conventional JTWPAs, evidenced by the later-occurring SNRi compression, but rather by the additional pump depletion from pump intermodulation byproducts and self-oscillation formation inside the Floquet TWPA, which will be discussed in Chapter 5. In future work, this parametric oscillation can be alleviated by tighter fabrication tolerance and better compensation of small resonance variations from varying capacitive couplings, which will increase parametric oscillation threshold and potentially lead to a P_{1dB} closer to theory. Furthermore, this particular Floquet TWPA device has a measured critical current density J_c 17.7% smaller than the design value. With better J_c targeting, P_{1dB} will not only improve from higher junction critical current and input pump power, but also from reduced impedance mismatch and the resulting higher parametric oscillation threshold. In addition, P_{1dB} can also be improved with longer junction chains with proportionally larger critical currents.

Chapter 5

Intrinsic Quantum Efficiency using wQED calibration

We evaluate the intrinsic noise performance of our Floquet TWPA using a waveguide quantum electrodynamics (wQED) method [73, 87, 29, 88]. The wQED device, consisting of a qubit symmetrically coupled to a transmission line, provides an absolute power reference at the cryogenic stage at the qubit frequency for noise characterization. At weak coherent drive powers ($|\alpha|^2 \ll 1$ where α is the coherent state amplitude), the qubit absorbs a single photon from the drive field and emits a photon bidirectionally with a π phase shift, thereby perfectly reflecting the single photon through constructive interference in the backward direction and destructive interference in the forward direction [29, 88]. At higher drive powers, the transmission increases and approaches unity. The power-dependent transmission can thus be fitted to extract the desired absolute power reference.

5.1 Waveguide QED transmission calibration

The wQED device consists of a symmetric qubit coupled to an open transmission line, which functions as a waveguide. The qubit frequency can be tuned with a DC magnetic flux bias to find a flux-insensitive sweet spot, in this case 6.59 GHz. Once tuned to the desired qubit frequency, we perform a 2D scan of the transmission profile

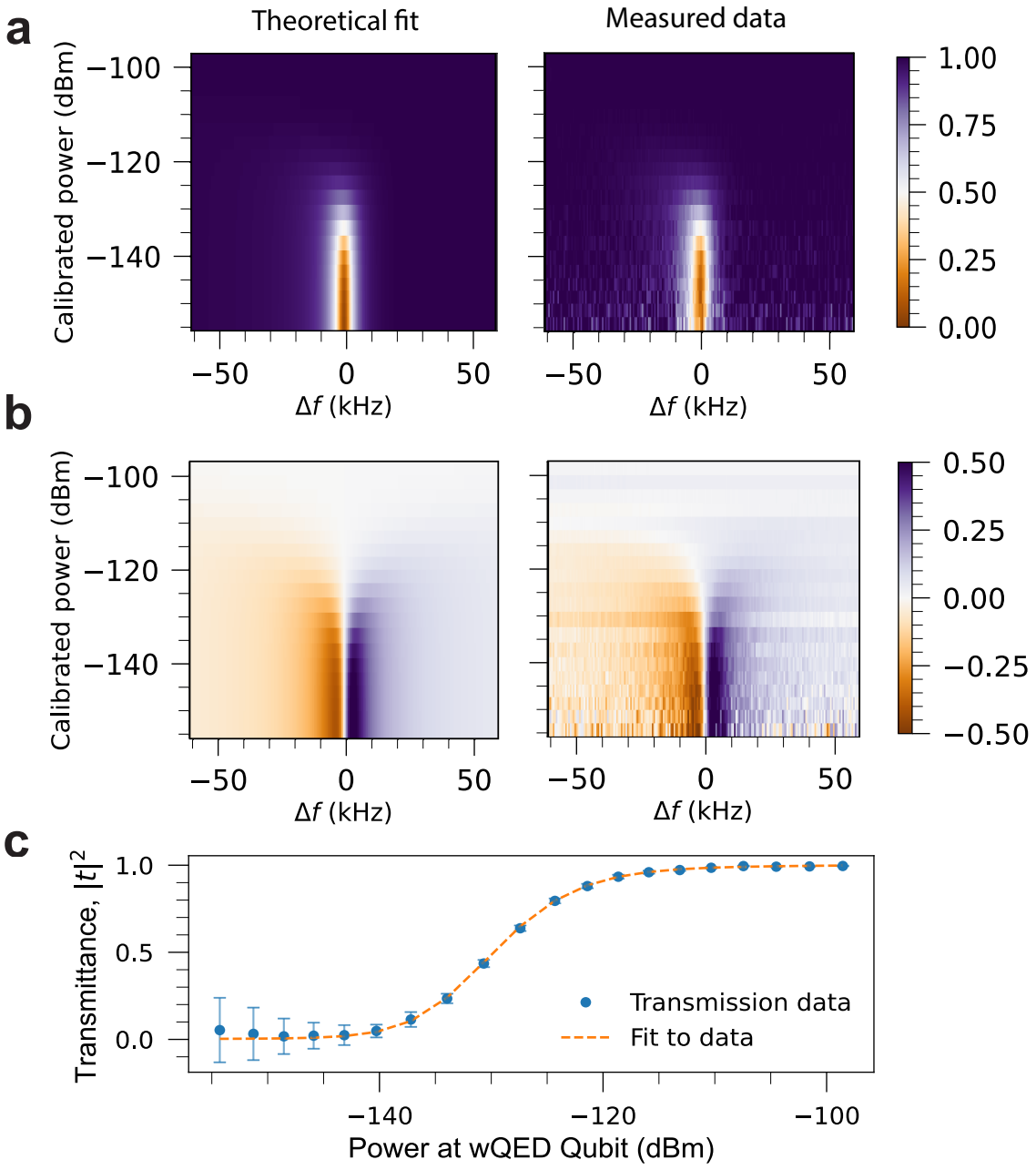

Figure 5-1: (a) Real part of theoretical model and real part of transmission data, in which we observe the qubit perfectly reflecting an input photon at low powers, versus transmitting near unity at higher powers. (b) Imaginary part of theoretical model and imaginary part of transmission data, where we see a phase shift corresponding to the dip in (a). (c) Global fit gives us a transmittance curve at the resonator frequency, which allows us to extract the absolute power at every nominal input power used for the power sweep.

by sending in a weak coherent drive at varying input powers. At lower drive powers, the qubit will absorb a single photon from the drive field and emit a photon bidirectionally with a π phase shift, thereby perfectly reflecting the single photon through constructive interference in the backwards direction and destructive interference in the forward direction. This results in a dip in the transmission at the resonant frequency. At higher drive powers, the higher number states of the qubit become excited and the resonant transmission increases, since the qubit can only emit up to a single photon. In Figure 5-1 (a) and (b), we note that the real and imaginary parts of the linear power scan exhibit the transmission behavior we expect (the measured data is normalized to transmission with the qubit far detuned). The equation describing transmission for a strongly coupled qubit and waveguide is

$$t = 1 - \frac{\Gamma_1}{2\Gamma_2} \frac{1 - \frac{i\Delta}{\Gamma_2}}{1 + \left(\frac{\Delta}{\Gamma_2}\right)^2 + \frac{\Omega^2}{\Gamma_1 \Gamma_2}}. \tag{5.1}$$

where Γ_1 is the decay rate of the qubit into the transmission line, Γ_2 is the transverse decoherence rate of the qubit, and Ω is the drive amplitude in units of Hz [29]. The absolute drive power at the qubit is given by [73]:

$$P = \pi \hbar \omega_i \Omega^2 / 2\Gamma_1. \tag{5.2}$$

By performing a global fit of the input power-dependent transmission as shown in Figure 5-1 (c), we can extract the drive amplitude Ω and the decay rate of the qubit into the transmission line Γ_1, and thus calculate the absolute power at the input of the wQED device and the Floquet TWPA, which we called reference plane **A** from the derivation in Chapter 2.

5.2 Measured intrinsic quantum efficiency

Figure 5-2(a) shows the experimental setup used to characterize the intrinsic amplifier quantum efficiency. The Floquet TWPA and the wQED device are placed in parallel

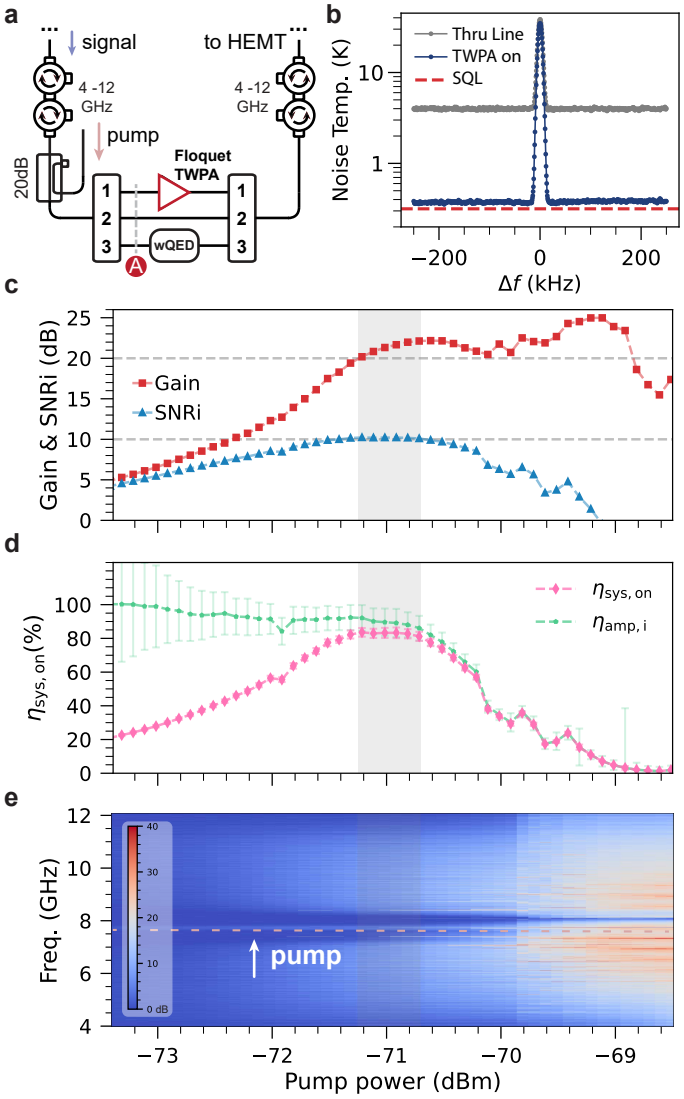

Figure 5-2: (a) Measurement setup for performing wQED power calibration and characterizing the intrinisic amplifier quantum efficiency. The plane of absolute power reference is placed right before the wQED and the Floquet TWPA within the switch bank, labeled by the red letter **A**. (b) Noise temperatures measured at the optimal pump configuration with the Floquet TWPA turned on (blue) and with it switched out (gray), respectively. The red dashed line corresponds to the standard quantum limit (SQL). Data is taken at a signal frequency of 6.59 GHz. (c) The measured gain and SNRi (see main text for definition) of the Floquet JTWPA as a function of the applied pump power at pump frequency 7.71 GHz. The optimal pump operating region is highlighted in light gray, within which the maximal SNRi of 10.23 dB occurs at a parametric gain of 20.18 dB. (d) The extracted system measurement efficiency $\eta_{\mathrm{sys,on}}$ (pink) and intrinsic amplifier quantum efficiency $\eta_{\mathrm{amp,i}}$ (green), respectively, with maximal values of $83.6\pm2.6\%$ and $92.1\pm7.6\%$. (e) The measured noise power spectra, normalized by the small-pump-power noise powers, as a function of the applied pump power on the decibel scale. The dashed line at 7.71 GHz corresponds to the applied pump as indicated by the white arrow and text. An abrupt noise floor rise is visible at around -69.85 dBm, indicative of the onset of self-oscillations in the Floquet TWPA.

inside a pair of multi-throw microwave switches, and the pump is combined with the input signal tone through a 20 dB directional coupler before the switch bank. The wQED device thus provides a power reference at the reference plane **A**, and we use nominally identical microwave cables with matching lengths and similar PCB packaging to minimize line differences between the different switch bank paths. After the switch bank, the signal is routed to a double-junction circulator, a superconducting NbTi cable, and a high-electron-mobility transistor amplifier (HEMT) for further amplification at 4K. We choose to operate and obtain an absolute power at the flux sweet spot qubit frequency of 6.59 GHz, which is also near the center of the TWPA high gain band.

In Figure 5-2(c), we plot the measured parametric gain (red) and the associated SNR improvement (blue), $\mathrm{SNRi} \equiv \mathrm{SNR}_{\mathrm{twpa,on}}/\mathrm{SNR}_{\mathrm{thru}}$, as a function of the input pump power at the pump frequency 7.71 GHz. Instead of the common definition of SNRi relative to an undriven device, we define the SNRi relative to a through line, because this fairly represents the SNR improvement from adding the amplifier into the measurement chain for devices with insertion loss. The parametric gain increases monotonically with increasing pump power and reaches a local peak of 22.17 dB at a pump power of ~ -70.5 dBm before decreasing. The SNRi follows a similar trend and peaks at 10.23 dB with a parametric gain of 20.19 dB, occurring at a gain just 1.98 dB before the peak gain at the pump power ~ -71.2 dBm. The close proximity of the gain and the SNRi optima in our Floquet TWPA shows an improvement over conventional TWPAs, as predicted in [7] from more efficient sideband suppression.

In Figure 5-2(d), we show the corresponding system measurement efficiency

$$\eta_{\mathrm{sys,on}} = \frac{\hbar\omega}{k_B T_{\mathrm{sys,on}}} \tag{5.3}$$

and the deduced phase-preserving intrinsic amplifier quantum efficiency from Eq.2.7:

$$\eta_{\mathrm{amp,i}}(G) = \left(\frac{2}{\eta_{\mathrm{sys,on}}} - \frac{2}{G\eta_{\mathrm{sys,off}}} + \frac{1}{G}\right)^{-1} \Big/ \eta_{\mathrm{ideal}}(G) \tag{5.4}$$

where G is the amplifier power gain (in linear units), $\eta_{\mathrm{ideal}}(G) = 1/(2 - 1/G)$ [7]

is the quantum efficiency of an ideal phase-preserving quantum-limited amplifier at gain G, $\eta_{\text{sys,off}}$ refers to the system measurement efficiency when the Floquet TWPA is turned off. We note that in this definition, the intrinsic amplifier quantum efficiency is normalized by that of an ideal phase-preserving quantum-limited amplifier, with 100% corresponding to the standard quantum limit.

Between pump powers of -71.25 dBm and -70.7 dBm exists a region (highlighted in light gray) in which the system measurement efficiency exceeds 80% and the parametric gain exceeds 20 dB concurrently. The optimal system measurement efficiency reaches $\eta_{\text{sys,on}} = 83.6 \pm 2.6\%$, for which the downstream amplification chain (including the HEMT) contributes to $9.22 \pm 1.05\%$ of the inefficiencies. This is among the highest reported system measurement efficiencies [31], and we note that in contrast to Ref. [31], our system measurement efficiency is measured without any attenuators immediately before or after the amplifiers, which would otherwise improve impedance matching conditions. At low parametric gain, the intrinsic amplifier quantum efficiency approaches the quantum limit, within measurement uncertainty. At the same operating point for optimal system measurement efficiency and > 20 dB gain, the intrinsic amplifier quantum efficiency is $\eta_{\text{amp,i}} = 92.1 \pm 7.6\%$, to our knowledge the highest reported value in TWPAs [18, 19, 20, 21, 89]. Figure 5-2(b) shows the system noise temperature of 378 ± 25 mK and 3.99 ± 0.25 K when the Floquet TWPA is turned on (blue) and switched out (gray), respectively, at the optimal pump operating point discussed above.

For the discussions above, the system noise is referred to the input of the wQED device/the Floquet TWPA as shown in Figure 5-2(a). The choice of this plane of reference **A** is suitable for extracting the intrinsic amplifier quantum efficiency, as is the central focus of this section. Nonetheless, we note that the attained high system measurement efficiency $\eta_{\text{sys,on}} = 83.6 \pm 2.6\%$ shows the great promise of minimizing the insertion loss between the preamplifier and the quantum processor. In addition, the above analysis sheds light on the limiting factors at high system measurement efficiencies. As preamplifiers continue to advance in performance and become tightly integrated with qubits, noise from downstream measurement chain will soon dominate

and limit the attainable system measurement efficiency to be under $\sim 90\%$, even at a 20 dB preamplifier gain. Near-ideal quantum measurements require preamplifiers with higher gain, HEMTs with improved noise performance, or a second stage of near-quantum-limited amplifiers following preamplification.

Above a pump power of -70 dBm, there exists a region where the parametric gain increases to ≈ 25 dB while the SNRi decreases significantly. The SNRi becomes negative around -69 dBm and parametric gain decreases again. Figure 5-2(e) shows the corresponding noise power rise spectra, normalized by the small-pump-power noise powers, as a function of frequency and pump power. We observe that these high gain regions with poor noise performance are correlated with uniformly spaced noise peaks, which form symmetrically about the dispersion feature and become increasingly more prominent at higher parametric gain. At a pump power of ~ -69.85 dBm, beyond the optimal operating point, an abrupt noise floor rise occurs across the entire spectrum, indicative of the onset of parametric self-oscillations, and consistent with the sudden increase in measured parametric gain. We hypothesize that the noise peaks are caused by self-oscillations originating in an effective cavity in the middle of the Floquet TWPA, due to the varying phase-matching resonator frequencies. The self-oscillation effect is also exacerbated by the minimal insertion loss and imperfect critical current density targeting from fabrication ($\sim$17.7% difference between measured and designed J_c).

Chapter 6

System Quantum Efficiency using cQED calibration

To characterize the system measurement efficiency for qubit readout, we perform an in-situ power calibration using the measurement-induced dephasing method [72, 18] on the transmon and readout resonator. A coherent tone populates the resonator, causing an AC Stark shift and measurement-induced dephasing of the qubit. We obtain an absolute power reference at the input of the qubit readout resonator by fitting to the functional dependence of these rates on the resonator drive power and detuning. Then, we can reliably calibrate the photon population in the resonator and consequently the absolute power reference for the measurement tone at the input of the qubit chip at the mixing chamber.

6.1 Circuit QED dephasing calibration

Figure 6-1 shows the pulse sequence of the aforementioned circuit QED power calibration method. This sequence is similar to the well-known Ramsey measurement, except that an additional weak measurement pulse with varying power is introduced between the two $\pi/2$ pulses instead of simply idling as in the Ramsey sequence. With a drive Hamiltonian $\hat{\mathcal{H}}_d = \epsilon_d \hat{a} e^{i\omega_d t} + H.c.$, in which $H.c.$ stands for the Hermitian conjugate of the preceding term and ω_d is the frequency of the drive tone, the steady-

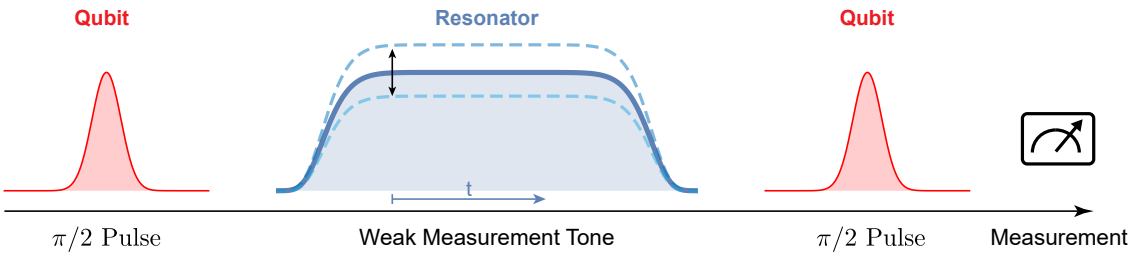

Figure 6-1: Pulse Sequence of the circuit-QED power calibration method. In each Ramsey-like measurement, the duration of the flat-top Gaussian weak measurement tone in between the two $\pi/2$ qubit pulses is varied to extract the measurement-induced dephasing rate and AC Stark shift from the decaying sinusoidals at a particular drive tone power. Such measurements are then repeated at varying input drive tone power for power calibration fitting.

state AC stark shift ω_{AC} and the measurement-induced dephasing rate Γ_m can be expressed as [72]

$$\begin{aligned} \omega_{AC} &= 2\chi \Re \alpha_e^* \alpha_g, \\ \Gamma_m &= 2\chi \Im \alpha_e^* \alpha_g, \end{aligned} \tag{6.1}$$

in which

$$\alpha_{e(g)} = \frac{-j\epsilon_d}{\kappa/2 + j(\Delta_r \pm \chi)}. \tag{6.2}$$

In the above formulae, $\Delta_r = \omega_{r0} - \omega_d$ is the resonator drive detuning, χ is the dispersive shift between the qubit and the resonator, ω_{r0} is the bare (uncoupled) resonant frequency of the resonator, and $\kappa = \kappa_{\text{int}} + \kappa_{\text{ext}}$ is the total or the loaded decay rate of the resonator. Utilizing the input-output theory, we can express the input power in the feedline with the external coupling rate κ_{ext} as

$$P_{\text{in}} = \hbar\omega_d \epsilon_d^2 / \kappa_{\text{ext}}. \tag{6.3}$$

Figure 6-2(a) shows the measured AC Stark Shift ω_{AC} and measurement-induced dephasing rate Γ_m as a function of the drive detuning Δ_r. Figure 6-2(b) shows three representative linecuts, in which the weak measurement tone is far-detuned, at $|1\rangle$ state resonance, and bare-resonance ω_{r0}, respectively. In the far-detuned case (Figure 6-2(b) top), the resonator is barely populated by the drive and thus has minimal excess dephasing. In contrast, the measurement-induced dephasing is maximized

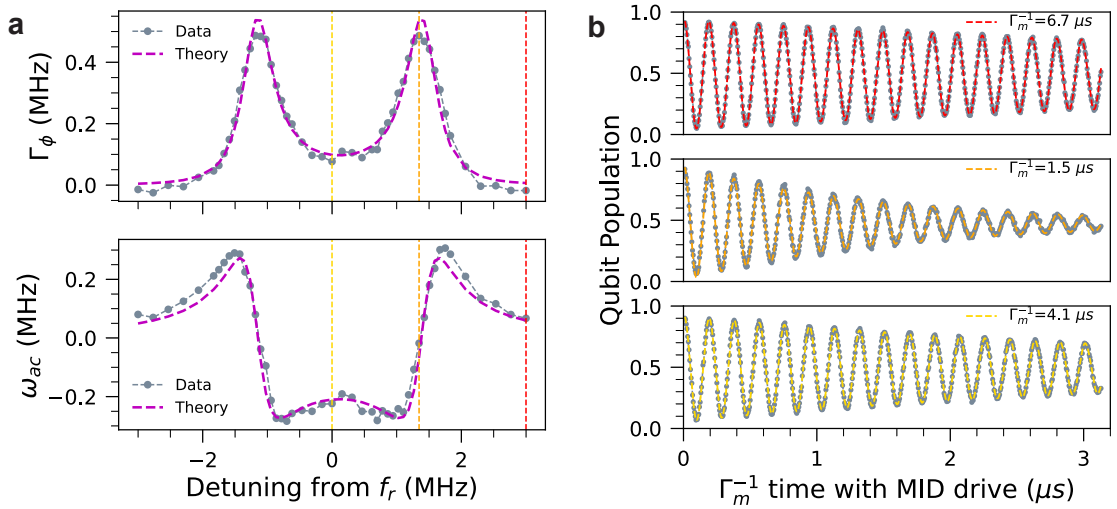

Figure 6-2: (a) The measurement-induced dephasing rate Γ_m and AC Stark Shift ω_{AC} as a function of the detuning $\Delta_r = \omega_{r0} - \omega_d$. (b) Measurement-induced dephasing Measurements (Figure 6-1) as a function of the dephasing pulse duration at far-detuned (top), near $|1\rangle$ state resonance (middle), and at bare resonance (bottom), respectively.

around the $|1\rangle$ resonance (Figure 6-2(b) bottom).

Figure 6-3 shows the measured AC Stark Shift ω_{AC} and measurement-induced dephasing rate Γ_m as a function of the DAC input power. We note the bottom x-axis values P_{DAC} (or MID pulse drive power) here are referenced at the input going into the fridge at room temperature and therefore do not correspond to the power at the chip to be calibrated, but instead act as a scaling reference for power linearity and fitting. The top x-axis corresponds to the power-calibrated number of photons in the resonator after fitting. The dashed-line fits in Figure 6-3 is obtained by applying the experimentally extracted parameters χ, ω_{r0}, and κ presented in Table 6.1 and using $c_\epsilon = \epsilon_d/\sqrt{P_{\mathrm{DAC}}}$ as the only free fitting parameter. We can then extract the photon number population and thus input measurement tone power at each nominal DAC input power reference from the simultaneous fit for ω_{AC} and Γ_m for use in noise characterization in the main text.

For the fits described above, we obtain the χ and κ values from resonator spectroscopy. Since this is a reflection measurement, it is possible to determine the external and internal losses by measuring the resonator transmission, shown in Fig. 6-4.

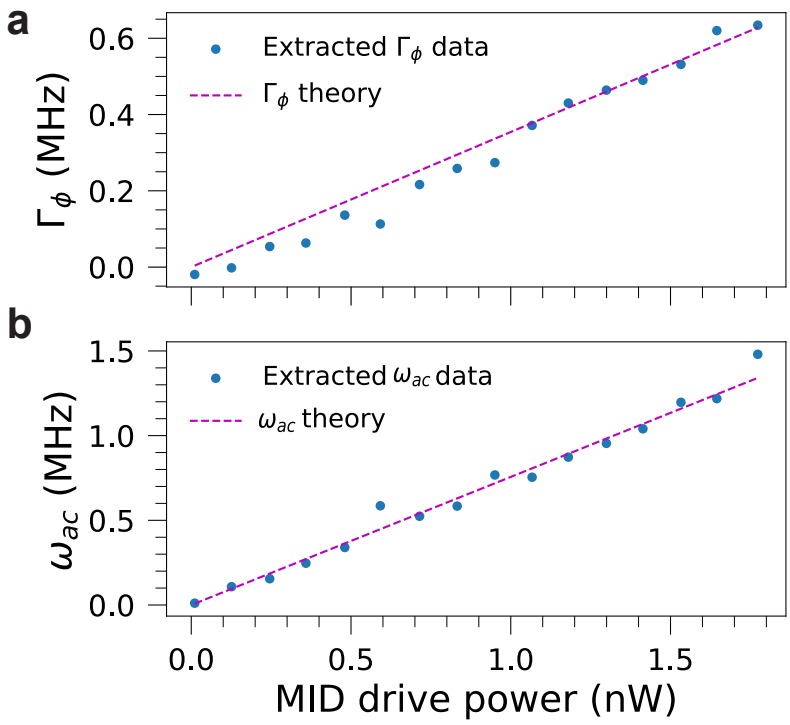

Figure 6-3: (a) The measurement-induced dephasing rate Γ_m (a) and AC Stark Shift ω_{AC} (b) as a function of the input DAC power at room temperature.

We utilize the following model for asymmetric resonators as follows [90, 91]:

$$S_{11}(f) = ae^{i\alpha}e^{-2\pi i f\tau}\left[\frac{(2Q_l/|Q_c|) + 2iQ_l\,(f/f_r - 1)}{1 - 2iQ_l\,(f/f_r - 1)}\right]. \tag{6.4}$$

From fitting the resonator transmission while the qubit is in the ground and excited states, we extract the values shown in Table. 6.1. We then input the χ and κ values into the theoretical fit for our measurement-induced dephasing frequency and power sweeps in Figure 6-2 and Figure 6-3. This allows us to extract a power factor ϵ_d from both sweeps at a chosen MID drive power, obtaining a difference of 5.293% between the two obtained factors; this leads to a difference of 0.45 dB in the absolute power calibration, -142.49 dBm and -142.04 dBm respectively. For the cQED power calibration in this work, we choose the value obtained from the frequency detuning MID sweep Figure 6-2 since it is a direct, well-averaged measurement over 49 different frequency points at our desired drive power, as opposed to a single frequency for the power-dependent MID sweep in Figure 6-3.

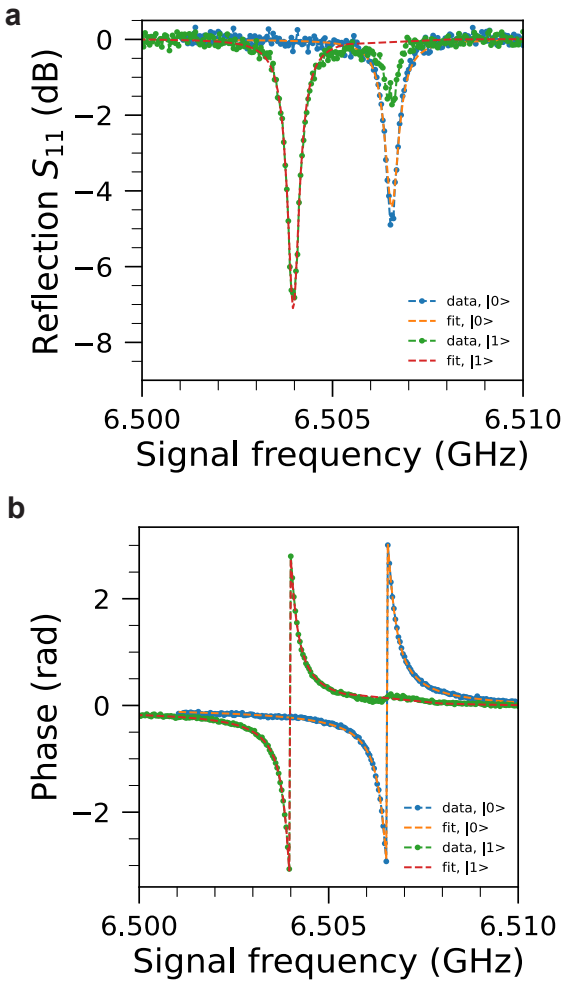

Figure 6-4: Resonator spectroscopy performed with qubit in ground (blue data, orange fit) versus excited (green data, red fit) states. Panel a) is the reflection and panel b) is the phase.

Table 6.1: Circuit QED parameters of the qubit-resonator system used for power calibration.

ω_q (GHz)	ω_{r0} (GHz)	χ (MHz)	κ (MHz)	κ_{ext} (MHz)
5.769	6.505	1.296 ± 0.03	0.572 ± 0.04	0.458 ± 0.002

6.2 Measured full-chain system quantum efficiency

We now use the Floquet TWPA in a qubit readout experiment. As shown in **??**(a), we perform a reflection measurement on a transmon qubit separated from the TWPA by a single-junction circulator and a 20-dB directional coupler. A circulator after the Floquet TWPA mitigates reflections from subsequent components and reduces thermal noise from higher temperature stages.

We perform noise spectral power density measurements and extract the maximum system efficiency to be $65.1\% \pm 5.8\%$, at 20.6 dB gain, depicted in Figure 6-5(b). This measurement efficiency is significantly higher than previously reported qubit-readout-chain measurement efficiencies using TWPAs of approximately 20% to 50% [18, 71, 92, 93, 94, 95, 20, 96], and is among the best achieved by phase-preserving Josephson parametric amplifiers (JPAs), ranging from 55% to 63% for similar readout chains [42, 41, 52, 53, 51, 97, 98]. We note that when operated in phase-sensitive configurations, parametric amplifiers can provide higher system efficiencies [47, 45, 46, 43].

6.3 Projective qubit readout

With the TWPA pump on, we obtain representative single shot readout histograms in Fig. 6-5(c) and measure a T_1-limited readout fidelity of 97.23% on average, with a readout length of $0.5\,\mu$s. Overall, the Floquet TWPA provides an attractive balance of wide bandwidth, high gain, and low noise for applications such as multiplexed readout of superconducting or spin qubits [92, 94, 95, 11, 85].

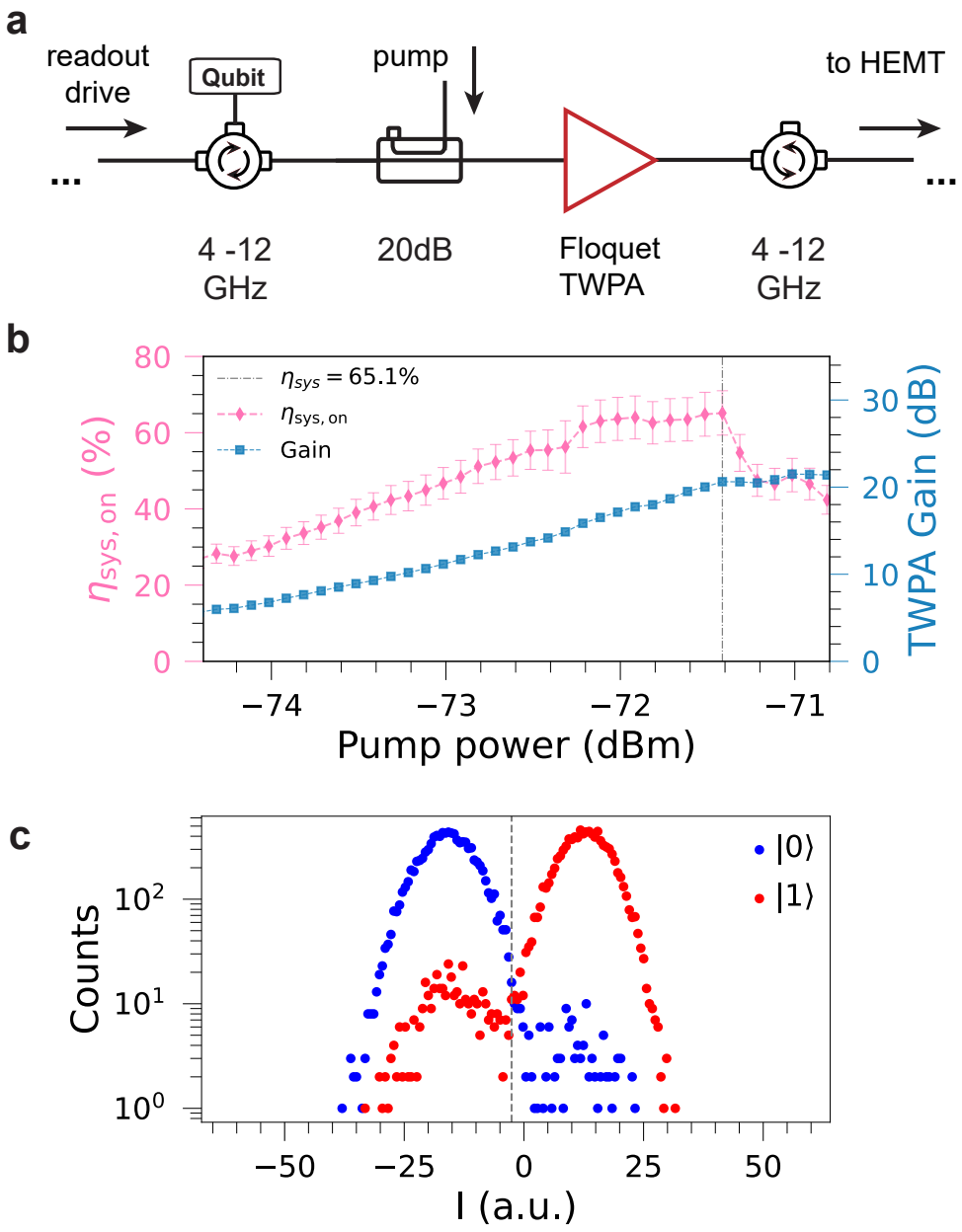

Figure 6-5: (a) Measurement setup for qubit readout, featuring a transmon qubit in reflection followed by the Floquet TWPA. (b) Using measurement-induced dephasing of the qubit, system efficiency is calculated to be $65.1\% \pm 5.8\%$ at max (pink dots). At the same pump power, the parametric gain is 20.6 dB (blue squares). (c) Qubit readout with the JTWPA pump on, resulting in an average readout fidelity of 97.23% over an integration time of 0.5 μs, with the threshold between the ground and excited states defined by the gray dashed line.

Chapter 7

Conclusion

In this work, we have presented the first experimental demonstration of a Floquet TWPA, featuring $> 20\,\mathrm{dB}$ parametric gain over 3 GHz of instantaneous bandwidth. Implemented using a standard superconducting qubit fabrication process, this Floquet TWPA has an average insertion loss of $< 0.5\,\mathrm{dB}$ within the 4-12 GHz band, which is among the lowest insertion losses reported for a JTWPA [18, 71, 92, 93, 94, 95, 97, 98, 46].

We have also performed precise calibrations of the power incident on the TWPA device using two different methods, one based on the AC stark shift of a strongly coupled reflection-style qubit, and one based on the input-power-dependent transmission of a wQED qubit coupled to an open transmission line. From these power calibration methods, we show that the Floquet TWPA is capable of reaching an intrinsic quantum efficiency of $\eta_{\mathrm{amp,i}} = 92.10 \pm 7.6\%$ at $> 20\,\mathrm{dB}$ parametric gain, which is the highest reported intrinsic quantum efficiency for phase-preserving parametric amplifiers in recent literature [18, 71, 92, 93, 94, 95, 46]. When situated in a superconducting qubit measurement setup as a general-purpose preamplifier, this Floquet TWPA enables a system measurement efficiency of $65.1 \pm 5.8\%$, the highest reported in a superconducting qubit readout experiment with a phase-preserving amplifier to the best of our knowledge [42, 41, 52, 53, 51, 97, 98].

Gain saturation measurements indicate that the Floquet JTWPA has $P_{\mathrm{1dB}} = -106.5$, which is typical for a JTWPA device[83] but lower than theoretical pre-

diction. The dynamic range and general noise performance of the Floquet JTWPA are adversely affected by the presence of pump intermodulation byproducts, which manifest as measurable features in the noise power spectra with a clear dependence on pump power. We hypothesize that these byproducts occur due to impedance mismatches from both fabrication and capacitative coupling variation across the device, which creates an intra-TWPA cavity susceptible to self-oscillatory behavior. We plan to address the parametric self-oscillations with improved J_c targeting, fabrication precision, and compensation for capacitive coupling variation across the device profile.

Furthermore, the qubit-compatible fabrication of the Floquet TWPA provides significant potential for reducing footprint and insertion loss in superconducting qubit readout chains. We propose patterning the qubit, directional coupler, and Floquet JTWPA on the same Al wafer, then integrating them into the same package; this will eliminate cabling between these devices, while still allowing for modularity with the option of wire or bump bonding individual devices. With these improvements, we intend to further enhance the performance of Floquet TWPAs to attain a projected $> 80\%$ measurement efficiency, with the goal of enabling large-scale fault-tolerant quantum computers and critical sensing applications in fundamental physics.

Appendix A

Full fridge diagram

We characterize the Floquet TWPA in this paper with two setups: first, in a switchbank optimized for extracting TWPA metrics referred to a through line, and second, in a qubit readout chain optimized for high system efficiency. The two setups are depicted in fig. A-1. For the first setup in fig. A-1 (a), the gain and insertion loss measurements, as well as the transmission measurements of the wQED device, are performed with a vector network analyzer (VNA; Hewlett Packard 8720ES). For noise rise experiments, we utilize an RF generator source (Windfreak; SynthHD PRO v2) for a clean signal tone with minimal sidebands, and inspect the SNR improvement on a spectrum analyzer (SA; Agilent E4440A). The TWPA pump tone is provided by a separate RF generator (Windfreak; SynthHD PRO v2) at room temperature, and couples into the signal line with a directional coupler (Marki; C20-0226) at cryogenic temperatures. The Floquet TWPA is situated in parallel with the wQED device and through line in a Radiall 6-port switchbank (Radiall R591762600); we utilize non-magnetic cables of the same length and make within the switchbank in order to provide the best possible reference for the line with the Floquet TWPA. The cables in the through line are connected with a SMPM barrel, as a close analog to the adapters used to interface between the SMA-connectorized non-magnetic cables and the TWPA package input with SMPM connectors. Before the directional coupler and after the switchbank, we have 4-12 GHz double junction isolators and circulators (LNF; ISISC4-12A, CICIC4-12A) to provide directionality and minimize the

effect of downstream reflections. The signal goes through a HEMT amplifier (LNF; LNC-6-20D), is further amplified by two room temperature amplifiers (Mini-Circuits ZX60-05113-LN+), and reaches room temperature readout, which in turn can go to port 2 of the VNA for transmission measurements, or the SA for noise rise experiments.

The setup in fig. A-1 (b) consists of a simple qubit readout chain, with a transmon qubit measured in reflection, utilizing the same fridge attenuation and TWPA pump source as in (a). To minimize heating from the TWPA pump tone, we add two bandpass filters (MCL VBF-7500+ 7450 to 7650 MHz BPF) to the pump line at the mixing chamber stage. Since this measurement chain is optimized for high system efficiency, we minimize the insertion loss between the qubit and the Floquet TWPA by using a single junction circulator (LNF; CICIC4-12A) along with a low-loss aluminium cable. In addition, we reduce the output circulator to a single junction circulator, and use a HEMT amplifier (LNF; LNC4-8C) that has a low noise temperature of 1.5 K. For transmission experiments, we likewise obtain data with the VNA. For qubit readout, power calibration, and noise rise experiments, the input signal tone is provided by a digital-to-analog-converter (DAC) pin of an FPGA (AMD Zynq UltraScale+ RFSoC ZCU111, Xilinx) running the Quantum Instrumentation Control Kit (QICK) software. The output tone is read out either by the native analog-to-digital converter (ADC) of the FPGA for qubit experiments, or with the SA for noise rise experiments.

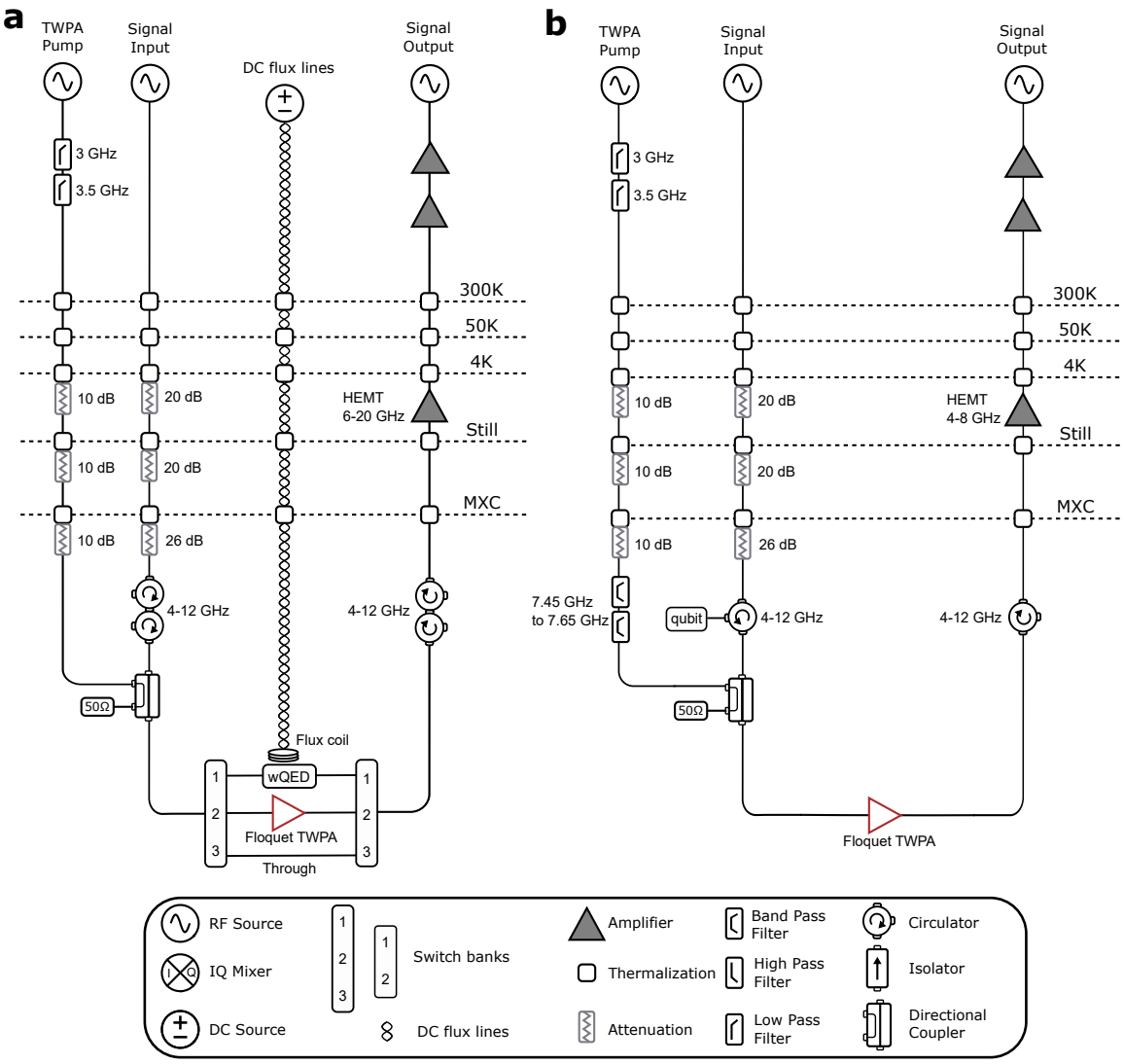

Figure A-1: (a) Fridge diagram for the setup to characterize gain, insertion loss, and intrinsic quantum efficiency performance metrics of the Floquet TWPA, including a through line and wQED device in parallel with the Floquet TWPA. (b) Fridge diagram for the setup to characterize Floquet TWPA performance in a qubit readout chain. The transmon qubit is measured in reflection and used to perform a power calibration (described in Appendix D) to obtain the measurement efficiency of the full system.

Appendix B

Packaging improvements

Initially, as shown in Fig. B-1, the JTWPA package consisted of a simple copper box with a groove in which to insert the chip, as well as a hole drilled underneath the JTWPA chip to effectively 'dilute' the permittivity of the substrate and thus increase the frequency of the package mode. However, upon first measurement of the package at room temperature, we discovered modes at 10, 17 and 22 to 25 GHz that would result in the signal bypassing the actual JTWPA chip upon cryogenic operation. Thus, we implemented two changes; first, by extending the center hole underneath the JTWPA chip to a trench underneath the interposer chips as well as the JTWPA chip, we pushed the modes up further to only around 22 GHz; next, we sealed the gaps between interposer chips and the ground plane with silver paste. In Fig. B-2 we show the room-temperature measurement results of these modifications.

We were guided to make these modifications by HFSS eigenmode simulations, which show where the higher-frequency modes are located in the device. For example, Fig. B-3 demonstrates that there are modes at 24.5 GHz located in the gap between the interposer chip and package body, which we then sealed with silver paste.

We note that there still exist nonidealities with this package design, namely, the soldered SMA-style connectors and wirebonds to the package introduce impedance mismatches to the system, and furthermore, there still exist modes as 26 GHz. The described design would be appropriate for initial testing at 23 GHz or below, but not for the final JTWPA implementation.

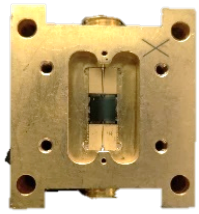

Figure B-1: Original JTWPA package design from MIT Lincoln Laboratory.

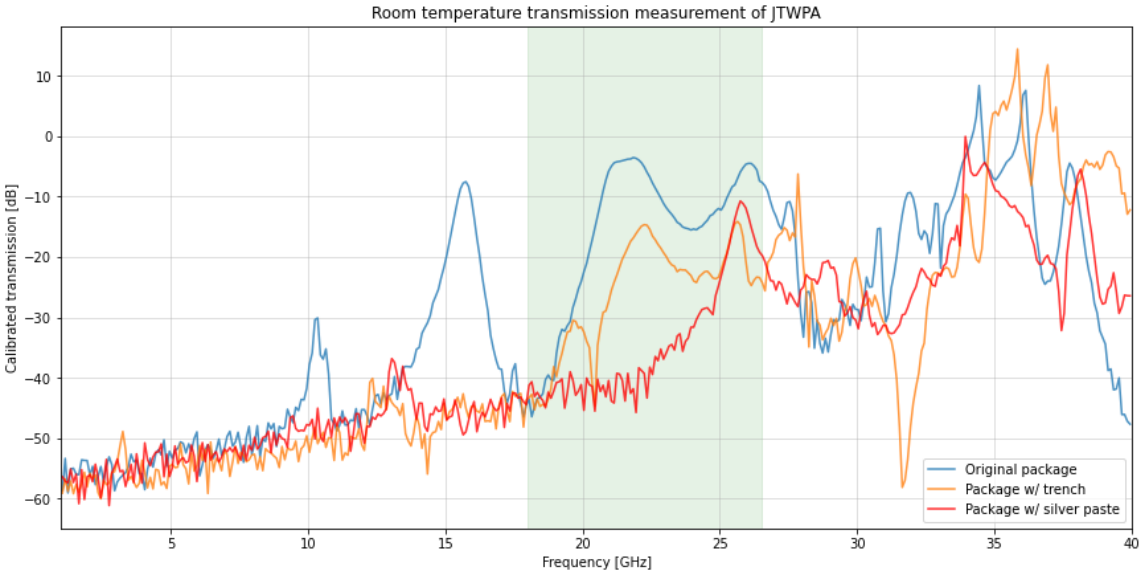

Figure B-2: Room temperature transmission measurement of original package (blue line), adding a larger trench to the package (orange line), and sealing gaps with silver paste (red line).

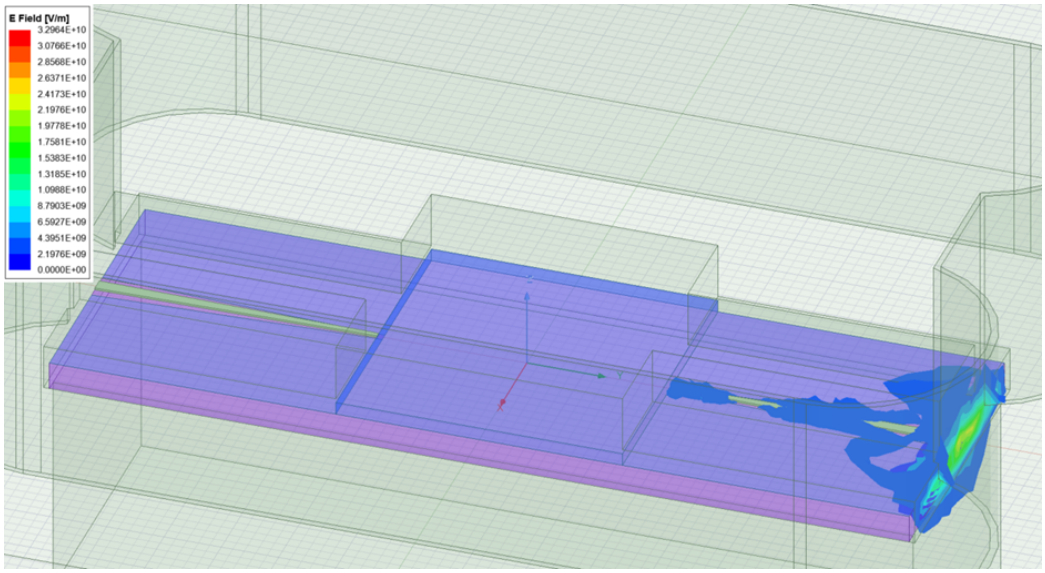

Figure B-3: Example 24.2 GHz mode in trenched package, not yet sealed with silver paste.

Thus, our group has developed a new package design that replaces the SMA connectors with SMPM connectors, rated up to 60 GHz at room temperature, and eliminates the need for wirebonding between the interposer and package. This improved design optimizes package and connector modes, minimizes wirebonds on interposer chips, and employs signal-line compensation strategies for better impedance matching up to 18 GHz.

Our new package design is outlined in Figure. B-4. The package base and lid are Copper 101, ordered from Protolabs and gold plated at MIT's T. J. Rodgers Laboratory for thermalization. Instead of a design in which the interposer chip and the device itself both have to be wirebonded to the base of the package, we use a copper/TMM10i interposer to hold the TWPA device above a trenched cutout. The PCB material is ordered from Rogers Corp. and laser cut using an LPKF ProtoLaser U4 machine, also at the T. J. Rodgers Laboratory. TMM10i was chosen for its thermal compatibility with the rest of the package, and we are able to gold plate the PCB for better wirebonding quality if needed. To provide the grounding of the PCB and as well as the chip, we add a ring of indium wire that holds the PCB in place once the lid is firmly screwed on. This enables greater modularity and faster testing, as

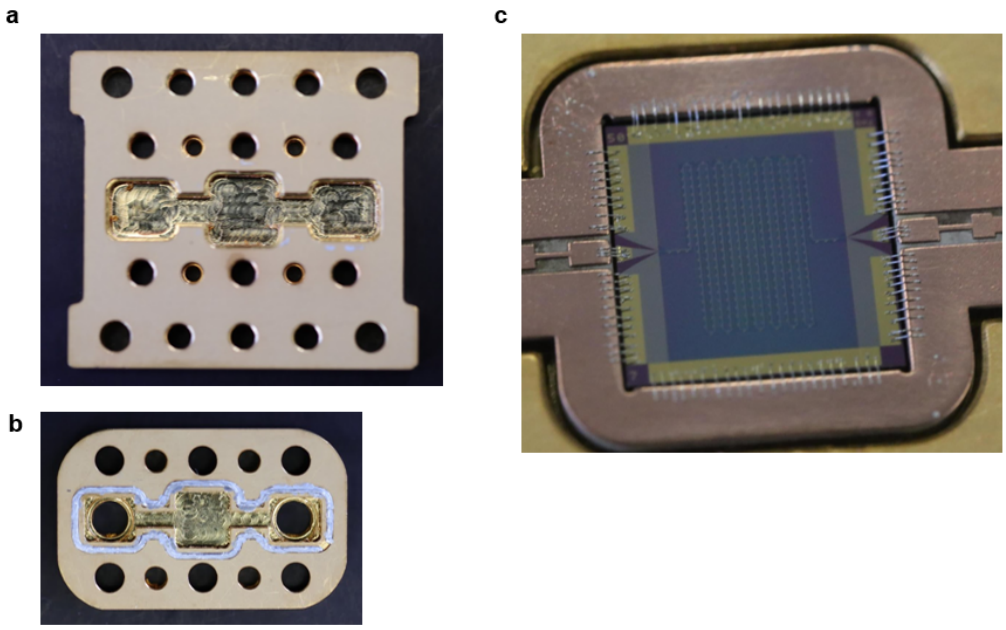

Figure B-4: New package design, featuring (a) base, (b) lid, and (c) a picture of the encapsulated PCB holding a wirebonded 5x5 uniform JTWPA chip. Note the compensation structures on the PCB that help mitigate impedance mismatches caused by the wirebonds.

we can easily swap out devices and cool down the same package without having to remove wirebonds.

To improve impedance matching for the whole package at a wide range of frequencies, we switch to SMPM connectors from Samtec (rated up to 40 GHz operation) instead of SMA connectors, and we iterate the optimal footprint design to cut out on the PCB with EM simulation software Ansys HFSS. We also model the impedance mismatch caused by the wirebonds between the PCB and the TWPA device, and compensate for the additional inductance by adding a Chebysheve filter on the interposer coplanar waveguide, as pictured in Fig. B-4(c).

Our design improvements lead to easily scaled designs, such as the 5x40 mm chip package used for the Floquet JTWPAs in this thesis, pictured in Fig. B-5(a). We measured the room temperature modes of two of these packages using a simple CPW in place of the JTWPA devices, and demonstrate that they are well matched up to a frequency of 15 - 18 GHz in Fig. B-5(b), which is a marked improvement over

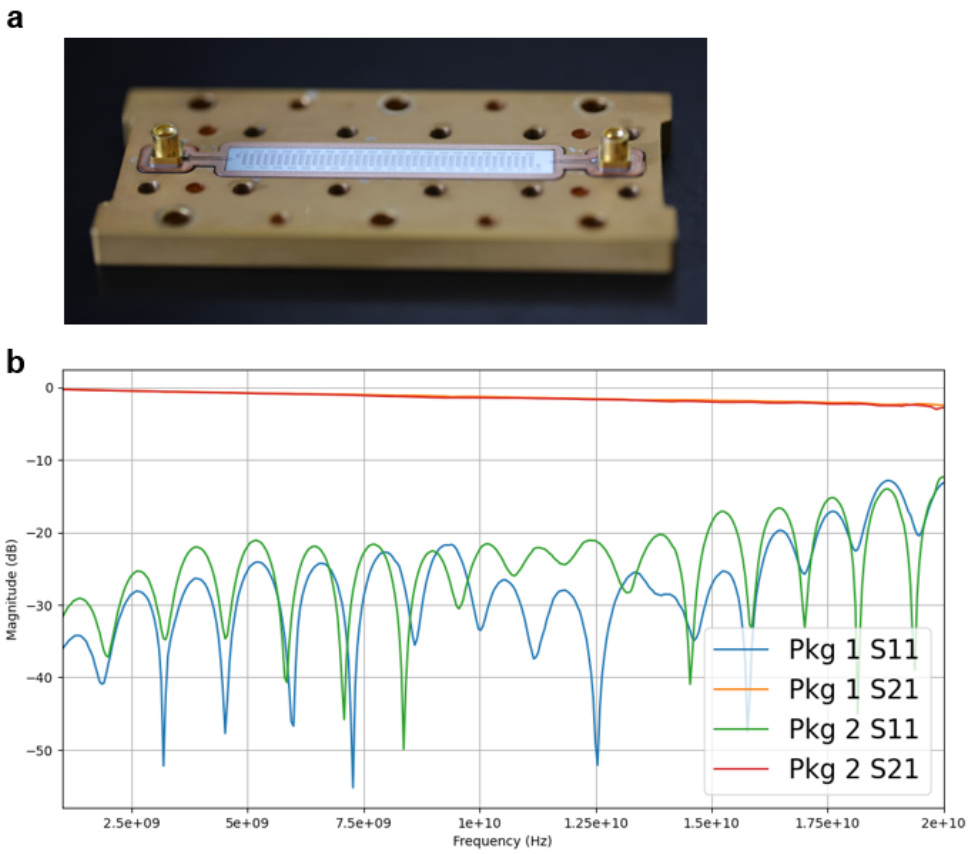

Figure B-5: (a) New package design for the 5x40 mm Floquet JTWPA chip. (b) Room temperature measurements of the new package using a simple CPW spacer chip show reflections under -20 dB below 15 to 18 GHz.

the previous design. Since this design features low reflection and minimal spurious modes over a broad range of frequencies, this package can also be tailored to suit a wide range of superconducting quantum devices, and we have tested additional packages for qubits (with added flux lines) that we intend to integrate with JTWPA packages in future work.

Bibliography

[1] Kaidong Peng. *The Quest for Ideal Quantum Amplifiers*. PhD thesis, Massachusetts Institute of Technology, 2023.

[2] L. Fasolo, A. Greco, and E. Enrico. Superconducting josephson-based metamaterials for quantum-limited parametric amplification: a review. *Intech Open: Condensed Matter Physics*, 2019.

[3] James William Rohlf. Modern physics from a to z. *Wiley*, 1994.

[4] P. Krantz, M. Kjaergaard, F. Yan, T. P. Orlando, S. Gustavsson, and W. D. Oliver. A quantum engineer's guide to superconducting qubits. *Appl. Phys. Rev. 1*, 6 (2):021318, 2019.

[5] O. Yaakobi, L. Friedland, C. Macklin, and I. Siddiqi. Parametric amplification in josephson junction embedded transmission lines. *Phys. Rev. B*, 87:144301, 2013.

[6] Kevin O'Brien, Chris Macklin, Irfan Siddiqi, and Xiang Zhang. Resonant phase matching of josephson junction traveling wave parametric amplifiers. *Phys. Rev. Lett.*, 113:157001, Oct 2014.

[7] Kaidong Peng, Mahdi Naghiloo, Jennifer Wang, Gregory D. Cunningham, Yufeng Ye, and Kevin P. O'Brien. Floquet-mode traveling-wave parametric amplifiers. *PRX Quantum*, 3:020306, Apr 2022.

[8] Carlton M. Caves. Quantum limits on noise in linear amplifiers. *Phys. Rev. D*, 26:1817–1839, Oct 1982.

[9] François Mallet, Florian R. Ong, Agustin Palacios-Laloy, François Nguyen, Patrice Bertet, Denis Vion, and Daniel Esteve. Single-shot qubit readout in circuit quantum electrodynamics. *Nature Physics*, 5(11):791–795, Nov 2009.

[10] Z. R. Lin, K. Inomata, W. D. Oliver, K. Koshino, Y. Nakamura, J. S. Tsai, and T. Yamamoto. Single-shot readout of a superconducting flux qubit with a flux-driven josephson parametric amplifier. *Applied Physics Letters*, 103(13):132602, 09 2013.

[11] Sebastian Krinner, Nathan Lacroix, Ants Remm, Agustin Di Paolo, Elie Genois, Catherine Leroux, Christoph Hellings, Stefania Lazar, Francois Swiadek, Johannes Herrmann, Graham J. Norris, Christian Kraglund Andersen, Markus

Müller, Alexandre Blais, Christopher Eichler, and Andreas Wallraff. Realizing repeated quantum error correction in a distance-three surface code. *Nature*, 605(7911):669–674, May 2022.

[12] A Yu Kitaev. Quantum computations: algorithms and error correction. *Russian Mathematical Surveys*, 52(6):1191, dec 1997.

[13] S. B. Bravyi and A. Yu. Kitaev. Quantum codes on a lattice with boundary. *Preprint at https://arxiv.org/abs/quant-ph/9811052*, 1998.

[14] Eric Dennis, Alexei Kitaev, Andrew Lahl, and John Preskill. Topological quantum memory. *Journal of Mathematical Physics*, 43(9):4452–4505, 08 2002.

[15] A.Yu. Kitaev. Fault-tolerant quantum computation by anyons. *Annals of Physics*, 303(1):2–30, 2003.

[16] Jack Edmonds. Paths, trees, and flowers. *Canadian Journal of Mathematics*, 17:449–467, 1965.

[17] Jack Edmonds. Maximum matching and a polyhedron with 0, 1-vertices. *Journal of research of the National Bureau of St and ards B*, 69(125-130):55–56, 1965.

[18] C. Macklin, K. O'Brien, D. Hover, M. E. Schwartz, V. Bolkhovsky, X. Zhang, W. D. Oliver, and I. Siddiqi. A near–quantum-limited Josephson traveling-wave parametric amplifier. *Science*, 350(6258):307–310, Oct 2015.

[19] T. C. White, J. Y. Mutus, I.-C. Hoi, R. Barends, B. Campbell, Yu Chen, Z. Chen, B. Chiaro, A. Dunsworth, E. Jeffrey, J. Kelly, A. Megrant, C. Neill, P. J. J. O'Malley, P. Roushan, D. Sank, A. Vainsencher, J. Wenner, S. Chaudhuri, J. Gao, and John M. Martinis. Traveling wave parametric amplifier with Josephson junctions using minimal resonator phase matching. *Appl. Phys. Lett.*, 106(24):242601, Jun 2015.

[20] Luca Planat, Arpit Ranadive, Rémy Dassonneville, Javier Puertas Martínez, Sébastien Léger, Cécile Naud, Olivier Buisson, Wiebke Hasch-Guichard, Denis M. Basko, and Nicolas Roch. Photonic-Crystal Josephson Traveling-Wave Parametric Amplifier. *Physical Review X*, 10(2):021021, April 2020. Publisher: American Physical Society.

[21] Arpit Ranadive, Martina Esposito, Luca Planat, Edgar Bonet, Cécile Naud, Olivier Buisson, Wiebke Guichard, and Nicolas Roch. Kerr reversal in josephson meta-material and traveling wave parametric amplification. *Nature Communications*, 13(1):1737, Apr 2022.

[22] Victor Gaydamachenko, Christoph Kissling, and Lukas Grünhaupt. An rf-SQUID-based traveling-wave parametric amplifier with -84 dBm input saturation power across more than one octave bandwidth. *Preprint at https://doi.org/10.48550/arXiv.2503.02489*, 2025.

[23] B. Yurke, L. R. Corruccini, P. G. Kaminsky, L. W. Rupp, A. D. Smith, A. H. Silver, R. W. Simon, and E. A. Whittaker. Observation of parametric amplification and deamplification in a Josephson parametric amplifier. *Phys. Rev. A*, 39(5):2519–2533, Mar 1989.

[24] T. Yamamoto, K. Inomata, M. Watanabe, K. Matsuba, T. Miyazaki, W. D. Oliver, Y. Nakamura, and J. S. Tsai. Flux-driven Josephson parametric amplifier. *Appl. Phys. Lett.*, 93(4):042510, Jul 2008.

[25] M. A. Castellanos-Beltran and K. W. Lehnert. Widely tunable parametric amplifier based on a superconducting quantum interference device array resonator. *Appl. Phys. Lett.*, 91(8):083509, Aug 2007.

[26] J. Y. Mutus, T. C. White, R. Barends, Yu Chen, Z. Chen, B. Chiaro, A. Dunsworth, E. Jeffrey, J. Kelly, A. Megrant, C. Neill, P. J. J. O'Malley, P. Roushan, D. Sank, A. Vainsencher, J. Wenner, K. M. Sundqvist, Clel, A. N. , and John M. Martinis. Strong environmental coupling in a Josephson parametric amplifier. *Appl. Phys. Lett.*, 104(26):263513, Jul 2014.

[27] Tanay Roy et al. Broadb and parametric amplification with impedance engineering: Beyond the gain-b and width product. *Appl. Phys. Lett.*, 107(26):262601, Dec 2015.

[28] Theodore White, Alex Opremcak, George Sterling, Alexander Korotkov, Daniel Sank, Rajeev Acharya, Markus Ansmann, Frank Arute, Kunal Arya, Joseph C. Bardin, Andreas Bengtsson, Alexandre Bourassa, Jenna Bovaird, Leon Brill, Bob B. Buckley, David A. Buell, Tim Burger, Brian Burkett, Nicholas Bushnell, Zijun Chen, Ben Chiaro, Josh Cogan, Roberto Collins, Alexander L. Crook, Ben Curtin, Sean Demura, Andrew Dunsworth, Catherine Erickson, Reza Fatemi, Leslie Flores Burgos, Ebrahim Forati, Brooks Foxen, William Giang, Marissa Giustina, Alejandro Grajales Dau, Michael C. Hamilton, Sean D. Harrington, Jeremy Hilton, Markus Hoffmann, Sabrina Hong, Trent Huang, Ashley Huff, Ivel, Justin , Evan Jeffrey, Mária Kieferová, Seon Kim, Paul V. Klimov, Fedor Kostritsa, John Mark Kreikebaum, L, David huis, Pavel Laptev, Lily Laws, Kenny Lee, Brian J. Lester, Alex Lill, er, Wayne Liu, Aditya Locharla, Erik Lucero, Trevor McCourt, Matt McEwen, Xiao Mi, Kevin C. Miao, Shirin Montazeri, Alexis Morvan, Matthew Neeley, Charles Neill, Ani Nersisyan, Jiun How Ng, Anthony Nguyen, Murray Nguyen, Rebecca Potter, Chris Quintana, Pedram Roushan, Kannan Sankaragomathi, Kevin J. Satzinger, Christopher Schuster, Michael J. Shearn, Aaron Shorter, Vladimir Shvarts, Jindra Skruzny, W. Clarke Smith, Marco Szalay, Alfredo Torres, Bryan W. K. Woo, Z. Jamie Yao, Ping Yeh, Juhwan Yoo, Grayson Young, Ningfeng Zhu, Nicholas Zobrist, Yu Chen, Anthony Megrant, Julian Kelly, and Ofer Naaman. Readout of a quantum processor with high dynamic range Josephson parametric amplifiers. *Applied Physics Letters*, 122(1), 01 2023. 014001.

[29] Jack Y. Qiu, Arne Grimsmo, Kaidong Peng, Bharath Kannan, Benjamin Lienhard, Youngkyu Sung, Philip Krantz, Vladimir Bolkhovsky, Greg Calusine, David Kim, Alex Melville, Bethany M. Niedzielski, Jonilyn Yoder, Mollie E. Schwartz, Orl, Terry P. o, Irfan Siddiqi, Simon Gustavsson, Kevin P. O'Brien, and William D. Oliver. Broadband squeezed microwaves and amplification with a josephson travelling-wave parametric amplifier. *Nature Physics*, 19:706–713, Feb 2023.

[30] Kaidong Peng, Rick Poore, Philip Krantz, David E. Root, and Kevin P. O'Brien. X-parameter based design and simulation of josephson traveling-wave parametric amplifiers for quantum computing applications. In *2022 IEEE International Conference on Quantum Computing and Engineering (QCE)*, pages 331–340, 2022.

[31] C. W. Sandbo Chang, Arjan F. Van Loo, Chih-Chiao Hung, Yu Zhou, Shuhei Tamate, and Yasunobu Nakamura. Josephson traveling-wave parametric amplifier based on low-intrinsic-loss coplanar lumped-element waveguide, 2025.

[32] John Preskill. Quantum computing in the nisq era and beyond. *Quantum*, 2018.

[33] Ants Remm, Sebastian Krinner, Nathan Lacroix, Christoph Hellings, François Swiadek, Graham J. Norris, Christopher Eichler, and Andreas Wallraff. Intermodulation distortion in a josephson traveling-wave parametric amplifier. *Physical Review Applied*, 20(3), September 2023.

[34] The KATRIN Collaboration. Direct neutrino-mass measurement with sub-electronvolt sensitivity. *Nat. Phys.*, 18:160–166, Feb 2022.

[35] C. Bartram, T. Braine, and R. Cervantes et.al. Dark matter axion search using a josephson traveling wave parametric amplifier. *Rev Sci Instrum*, 94:044703, April 2023.

[36] A. Giachero, C. Barone, and M. et al. Borghesi. Detector array readout with traveling wave amplifiers. *J Low Temp Phys*, 209:658–666, Aug 2022.

[37] Cullen AL. Theory of the travelling wave parametric amplifier. *Proceedings of the IEE - Part B: Electronic and Communication Engineering*, 32:101–107, 1959.

[38] Manuel A. Castellanos-Beltran, Kent D. Irwin, Leila R. Vale, Gene C. Hilton, and Konrad W. Lehnert. B and width and dynamic range of a widely tunable josephson parametric amplifier. *IEEE Transactions on Applied Superconductivity*, 19(3):944–947, 2009.

[39] M.T. Bell and A. Samolov. Traveling wave parametric amplifier based on a chain of coupled asymmetric squids. *Phys. Rev. Applied*, 4(2):024014, 2015.

[40] Leonardo Ranzani, Guilhem Ribeill, Brian Hassick, and Kin Chung Fong. Wideb and josephson parametric amplifier with integrated transmission line transformer. In *2022 IEEE International Conference on Quantum Computing and Engineering (QCE)*, pages 314–319, 2022.

[41] Ryan Kaufman, Theodore White, Mark I Dykman, Andrea Iorio, George Stirling, Sabrina Hong, Alex Opremcak, Andreas Bengtsson, Lara Faoro, Joseph C Bardin, Tim Burger, Robert Gasca, and Ofer Naaman. Josephson parametric amplifier with Chebyshev gain profile and high saturation. *Preprint at https://arxiv.org/abs/2305.17816*, 2023.

[42] R. Kaufman, C. Liu, K. Cicak, B. Mesits, M. Xia, C. Zhou, M. Nowicki, J. Aumentado, D. Pekker, and M. Hatridge. Simple, High Saturation Power, Quantum-Limited, RF SQUID Array-Based Josephson Parametric Amplifiers. *Preprint at https://doi.org/10.48550/arXiv.2402.19435*, 2024.

[43] T. Walter, P. Kurpiers, S. Gasparinetti, P. Magnard, A. Potočnik, Y. Salathé, M. Pechal, M. Mondal, M. Oppliger, C. Eichler, and A. Wallraff. Rapid high-fidelity single-shot dispersive readout of superconducting qubits. *Phys. Rev. Appl.*, 7:054020, May 2017.

[44] S. Touzard, A. Kou, N. E. Frattini, V. V. Sivak, S. Puri, A. Grimm, L Frunzio, S. Shankar, and M. H. Devoret. Gated conditional displacement readout of superconducting qubits. *Phys. Rev. Lett.*, page 080502, 2019.

[45] F. Lecocq, L. Ranzani, G. A. Peterson, K. Cicak, X. Y. Jin, R. W. Simmonds, J. D. Teufel, and J. Aumentado. Efficient Qubit Measurement with a Nonreciprocal Microwave Amplifier. *Physical Review Letters*, 126(2):020502, 2021.

[46] Eric I. Rosenthal, Christian M. F. Schneider, Maxime Malnou, Ziyi Zhao, Felix Leditzky, Benjamin J. Chapman, Waltraut Wustmann, Xizheng Ma, Daniel A. Palken, Maximilian F. Zanner, Leila R. Vale, Gene C. Hilton, Jiansong Gao, Graeme Smith, Gerhard Kirchmair, and K. W. Lehnert. Efficient and low-backaction quantum measurement using a chip-scale detector. *Phys. Rev. Lett.*, 126:090503, Mar 2021.

[47] A. Eddins, J. M. Kreikebaum, D. M. Toyli, E. M. Levenson-Falk, A. Dove, W. P. Livingston, B. A. Levitan, L. C. G. Govia, A. A. Clerk, and I. Siddiqi. High-efficiency measurement of an artificial atom embedded in a parametric amplifier. *Phys. Rev. X*, page 011004, 2019.

[48] Bingcheng Qing, Long B. Nguyen, Xinyu Liu, Hengjiang Ren, William P. Livingston, Noah Goss, Ahmed Hajr, Trevor Chistolini, Zahra Pedramrazi, David I. Santiago, Jie Luo, and Irfan Siddiqi. Broadb and coplanar-waveguide-based impedance-transformed josephson parametric amplifier. *Phys. Rev. Res.*, 6:L012035, Feb 2024.

[49] K. Backes, D. Palken, S. Kenany, B. Brubaker, S. Cahn, A. Droster, G. Hilton, S. Ghosh, H. Jackson, S. Lamoreaux, A. Feder, K. Lehnert, S. Lewis, M. Malnou, R. Maruyama, N. Rapidis, M. Simanovskaia, S. Singh, D. Speller, I. Urdinaran, L. Vale, E. van Assendelft, K. van Bibber, and H. Wang. A quantum enhanced search for dark matter axions. *Nature.*, 590:226–227, Feb 2021.

[50] Caterina Braggio, Giulio Cappelli, Giovanni Carugno, Nicolò Crescini, Raffaele Di Vora, Martina Esposito, Antonello Ortolan, Luca Planat, Arpit Ranadive, Nicolas Roch, and Giuseppe Ruoso. A haloscope amplification chain based on a traveling wave parametric amplifier. *Rev Sci Instrum*, 93:094701, Sept 2022.

[51] S. V. Uchaikin, J. Kim, Ç. Kutlu, B. I. Ivanov, J. Kim, A. F. van Loo, Y. Nakamura, S. Ahn, S. Oh, M. Ko, and Y. K. Semertzidis. Josephson Parametric Amplifier Based Quantum Noise Limited Amplifier Development for Axion Search Experiments in CAPP. *Preprint at https://doi.org/10.48550/arXiv.2406.07899*, 2024.

[52] G. Bothara, S. Das, K. V. Salunkhe, Ch, M. , J. Deshmukh, M. P. Patankar, and R. Vijay. High-Fidelity QND Readout and Measurement Back-Action in a Tantalum-Based High-Coherence Fluxonium Qubit. *Preprint at https://doi.org/10.48550/arXiv.2501.16691*, 2025.

[53] Ç. Kutlu, A. F. van Loo, S. V. Uchaikin, A. N. Matlashov, D. Lee, S. Oh, J. Kim, W. Chung, Y. Nakamura, and Y. K. Semertzidis. Characterization of a Flux-Driven Josephson Parametric Amplifier with near Quantum-Limited Added Noise for Axion Search Experiments. *Supercond. Sci. Technol.*, 34:085013, 2021.

[54] B.H. Eom, P. K. Day, H.G. Leduc, and J. Zmuidzinas. Wideband, low-noise superconducting amplifier with high dynamic range. *Nat. Phys.*, 8:623–627, 2012.

[55] S. Chaudhuri, D. Li, K. D. Irwin, C. Bockstiegel, J. Hubmayr, J. N. Ullom, M. R. Vissers, and J. Gao. Broadband parametric amplifiers based on nonlinear kinetic inductance artificial transmission lines. *Appl. Phys. Lett.*, 110(15):152601, 2017.

[56] M. Malnou, M.R. Vissers, J.D. Wheeler, J. Aumentado, J. Hubmayr, J.N. Ullom, and J. Gao. Three-wave mixing kinetic inductance traveling-wave amplifier with near-quantum-limited noise performance". *PRX Quantum*, 2:010302, 2021.

[57] S. Shu, N. Klimovich, B. H. Eom, A. D. Beyer, R. Basu Thakur, H. G. Leduc, and P. K. Day. Nonlinearity and wide-band parametric amplification in a (nb,ti)n microstrip transmission line. *Phys. Rev. Res.*, 3:023184, Jun 2021.

[58] Farzad Faramarzi, Ryan Stephenson, Sasha Sypkens, Byeong H. Eom, Henry LeDuc, and Peter Day. A 4–8 ghz kinetic inductance traveling-wave parametric amplifier using four-wave mixing with near quantum-limited noise performance. *APL Quantum*, 1(3):036107, 2024.

[59] N. Zobrist, B.H. Eom, P. Day, B.A. Mazin, S.R. Meeker, B. Bumble, H.G. LeDuc, G. Coiffard, P. Szypryt, N. Fruitwala, I. Lipartito, and C. Bockstiegel. Wide-band parametric amplifier readout and resolution of optical microwave kinetic inductance detectors. *Appl. Phys. Lett.*, 115:042601, 2019.

[60] Martina Esposito, Arpit Ranadive, Luca Planat, and Nicolas Roch. Perspective on traveling wave microwave parametric amplifiers. *Appl. Phys. Lett.*, 119:120501, Sept 2021.

[61] C. Kissling, V. Gaydamachenko, F. Kaap, M. Khabipov, R. Dolata, A. B. Zorin, and L. Grünhaupt. Vulnerability to parameter spread in josephson traveling-wave parametric amplifiers. *IEEE Transactions on Applied Superconductivity*, 33(5):1–6, 2023.

[62] A.B. Zorin. Josephson traveling-wave parametric amplifier with three-wave mixing. *Phys. Rev. Applied*, 6:034006, September 2016.

[63] A. Miano and O. A. Mukhanov. Symmetric traveling wave parametric amplifier. *IEEE Transactions on Applied Superconductivity*, 29(5):1–6, August 2019.

[64] Jennifer Wang*, Kaidong Peng*, Jeffrey M. Knecht, Gregory D. Cunningham, Andres E. Lombo, Alec Yen, Daniela A. Zaidenberg, Michael Gingras, Bethany M. Niedzielski, Hannah Stickler, Katrina Sliwa, Kyle Serniak, Mollie E. Schwartz, William D. Oliver, and Kevin P. O'Brien. High-efficiency, low-loss floquet-mode traveling wave parametric amplifier, 2025.

[65] Hampus Renberg Nilsson, Liangyu Chen, Giovanna Tancredi, Robert Rehammar, Daryoush Shiri, Filip Nilsson, Amr Osman, Vitaly Shumeiko, and Per Delsing. A small footprint travelling-wave parametric amplifier with a high signal-to-noise ratio improvement in a wide b and. *Preprint at https://doi.org/10.48550/arXiv.2408.16366*, 2024.

[66] M. Malnou, T. F. Q. Larson, J. D. Teufel, F. Lecocq, and J. Aumentado. Low-noise cryogenic microwave amplifier characterization with a calibrated noise source. *Review of Scientific Instruments*, 95(3):034703, 03 2024.

[67] Patrizia Livreri, Emanuele Enrico, Luca Fasolo, Angelo Greco, Alessio Rettaroli, David Vitali, Alfonso Farina, Francesco Marchetti, and Dario Giacomin. Intermodulation distortion in a josephson traveling wave parametric amplifier. *arXiv:2111.03409 [quant-ph]*, Nov 2021.

[68] J. E. Fernandez. A noise-temperature measurement system using a cryogenic attenuator. *TMO Progress Report*, 42:1–9, 1998.

[69] Slawomir Simbierowicz, Visa Vesterinen, Joshua Milem, Aleksi Lintunen, Mika Oksanen, Leif Roschier, Leif Grönberg, Juha Hassel, David Gunnarsson, and Russell E. Lake. Characterizing cryogenic amplifiers with a matched temperature-variable noise source. *Review of Scientific Instruments*, 92(3):034708, 03 2021.

[70] Lafe Spietz, K. W. Lehnert, I. Siddiqi, and R. J. Schoelkopf. Primary electronic thermometry using the shot noise of a tunnel junction. *Science*, 300(5627):1929–1932, 2003.

[71] C. C. Bultink, B. Tarasinski, Ha, N. bæk, S. Poletto, N. Haider, D. J. Michalak, A. Bruno, and L. DiCarlo. General method for extracting the quantum efficiency of dispersive qubit readout in circuit qed. *Applied Physics Letters*, 112(9):092601, 2018.

[72] Jay Gambetta, Alex Blais, re, D. I. Schuster, A. Wallraff, L. Frunzio, J. Majer, M. H. Devoret, S. M. Girvin, and R. J. Schoelkopf. Qubit-photon interactions in a cavity: Measurement-induced dephasing and number splitting. *Phys. Rev. A*, 74:042318, Oct 2006.

[73] M. Mirhosseini, E. Kim, and X. et al Zhang. Cavity quantum electrodynamics with atom-like mirrors. *Nature*, 569:692–697, May 2019.

[74] Brian D. Josephson. Possible new effects in superconductive tunnelling. *Physics Letters*, 1(7):251–253, 1962.

[75] D. Rosenberg, D. Kim, R. Das, D. Yost, S. Gustavsson, D. Hover, P. Krantz, A. Melville, L. Racz, G. O. Samach, S. J. Weber, F. Yan, J. L. Yoder, A. J. Kerman, and W. D. Oliver. 3d integrated superconducting qubits. *npj Quantum Information*, 3(1), October 2017.

[76] R N. Das, J.L. Yoder, D. Rosenberg, D.K. Kim, D. Yost, J. Mallek, D. Hover, V. Bolkhovsky, A.J. Kerman, and W.D. Oliver. Cryogenic qubit integration for quantum computing. In *2018 IEEE 68th Electronic Components and Technology Conference (ECTC)*, pages 504–514, 2018.

[77] Bethany M. Niedzielski, David K. Kim, Mollie E. Schwartz, Danna Rosenberg, Greg Calusine, Rabi Das, Alexander J. Melville, Jason Plant, Livia Racz, Jonilyn L. Yoder, Donna Ruth-Yost, and William D. Oliver. Silicon hard-stop spacers for 3d integration of superconducting qubits. In *2019 IEEE International Electron Devices Meeting (IEDM)*, pages 31.3.1–31.3.4, 2019.

[78] D. Rosenberg, S. Weber, D. Conway, D. Yost, J. Mallek, G. Calusine, R. Das, D. Kim, M. Schwartz, W. Woods, J. L. Yoder, and W. D. Oliver. 3d integration and packaging for solid-state qubits. *Preprint at https://doi.org/10.48550/arXiv.1906.11146*, 2019.

[79] D. R. W. Yost, M. E. Schwartz, J. Mallek, D. Rosenberg, C. Stull, J. L. Yoder, G. Calusine, M. Cook, R. Das, A. L. Day, E. B. Golden, D. K. Kim, A. Melville, B. M. Niedzielski, W. Woods, A. J. Kerman, and W. D. Oliver. Solid-state qubits integrated with superconducting through-silicon vias. *npj Quantum Information*, 6(1), July 2020.

[80] Justin L. Mallek, Donna-Ruth W. Yost, Danna Rosenberg, Jonilyn L. Yoder, Gregory Calusine, Matt Cook, Rabindra Das, Alexandra Day, Evan Golden, David K. Kim, Jeffery Knecht, Bethany M. Niedzielski, Mollie Schwartz, Arjan Sevi, Corey Stull, Wayne Woods, Andrew J. Kerman, and William D. Oliver. Fabrication of superconducting through-silicon vias. *Preprint at https://doi.org/10.48550/arXiv.2103.08536*, 2021.

[81] G. J. Dolan. Offset masks for lift-off photoprocessing. *Applied Physics Letters*, 31(5):337–339, 09 1977.

[82] Zijun Chen, A. Megrant, J. Kelly, R. Barends, J. Bochmann, Yu Chen, B. Chiaro, A. Dunsworth, E. Jeffrey, J. Y. Mutus, P. J. J. O'Malley, C. Neill, P. Roushan, D. Sank, A. Vainsencher, J. Wenner, T. C. White, A. N. Cleland, and John M. Martinis. Fabrication and characterization of aluminum airbridges for superconducting microwave circuits. *Applied Physics Letters*, 104(5):052602, 02 2014.

[83] G. L. Gal, G. Butseraen, A. Ranadive, G. Cappelli, B. Fazliji, E. Bonet, E. Eyraud, L. Planat, and N. Roch. Gain Compression in Josephson Traveling-Wave Parametric Amplifiers. *Preprint at https://arxiv.org/abs/2502.03022*, 2025.

[84] S. Krinner, S. Storz, P. Kurpiers, P. Magnard, J. Heinsoo, R. Keller, J. Lütolf, C. Eichler, and Wallraff. Engineering cryogenic setups for 100-qubit scale superconducting circuit systems. *EPJ Quantum Technol.*, 6, 2019.

[85] V. Elhomsy, L. Planat, D. J. Niegemann, B. Cardoso-Paz, A. Badreldin, B. Klemt, V. Thiney, R. Lethiecq, E. Eyraud, M. C. Dartiailh, Bertr, B. , H. Niebojewski, C. Bäuerle, M. Vinet, T. Meunier, N. Roch, and M. Urdampilleta. Broadband Parametric Amplification for Multiplexed SiMOS Quantum Dot Signals. *Preprint at https://doi.org/10.48550/arXiv.2307.14717*, 2024.

[86] Per Kylemark, Henrik Sunnerud, Magnus Karlsson, Peter A., and rekson. Semi-analytic saturation theory of fiber optical parametric amplifiers. *Journal of Lightwave Technology*, 24:3471–3479, 2006.

[87] B. Kannan, D. L. Campbell, F. Vasconcelos, R. Winik, D. K. Kim, M. Kjaergaard, P. Krantz, A. Melville, B. M. Niedzielski, J. L. Yoder, T. P. Orl, o, S. Gustavsson, and W. D. Oliver. Generating spatially entangled itinerant photons with waveguide quantum electrodynamics. *Science Advances*, 6(41):eabb8780, 2020.

[88] B. Kannan, Y. Almanakly, A.and Sung, A. Di Paolo, D. A. Rower, J. Braumüller, A. Melville, B. M. Niedzielski, A. Karamlou, K. Serniak, A. Vepsäläinen, M. E. Schwartz, J. L. Yoder, R. Winik, J. I.-J. Wang, T. P. Orlando, S. Gustavsson, J. A. Grover, and W. D. Oliver. On-demand directional microwave photon emission using waveguide quantum electrodynamics. *Nat. Phys.*, 19:394–400, 2023.

[89] Arpit Ranadive, Bekim Fazliji, Gwenael Le Gal, Giulio Cappelli, Guilliam Butseraen, Edgar Bonet, Eric Eyraud, Sina Böhling, Luca Planat, A. Metelmann,

and Nicolas Roch. A Traveling Wave Parametric Amplifier Isolator. *Preprint at https://doi.org/10.48550/arXiv.2406.19752*, 2024.

[90] S. Probst, F. B. Song, P. A. Bushev, A. V. Ustinov, and M. Weides. Efficient and robust analysis of complex scattering data under noise in microwave resonators. *Review of Scientific Instruments*, 86(2):024706, 02 2015.

[91] M. S. Khalil, M. J. A. Stoutimore, F. C. Wellstood, and K. D. Osborn. An analysis method for asymmetric resonator transmission applied to superconducting devices. *Journal of Applied Physics*, 111(5):054510, 03 2012.

[92] Johannes Heinsoo, Christian Kraglund Andersen, Ants Remm, Sebastian Krinner, Theodore Walter, Yves Salathé, Simone Gasparinetti, Jean-Claude Besse, Anton Potocnik, Andreas Wallraff, and Christopher Eichler. Rapid high-fidelity multiplexed readout of superconducting qubits. *Phys. Rev. Appl.*, 10:034040, Sep 2018.

[93] T. Peronnin, D. Markovic, Q. Ficheux, and B. Huard. Sequential dispersive measurement of a superconducting qubit. *Phys. Rev. Lett.*, 124:180502, May 2020.

[94] C. K. Andersen, A. Remm, S. Lazar, S. Krinner, J. Heinsoo, J.-C. Besse, M. Gabureac, A. Wallraff, and C Eichler. Entanglement stabilization using ancilla-based parity detection and real-time feedback in superconducting circuits. *npj Quantum Inf*, 5:1–7, 2019.

[95] C. K. Andersen, A. Remm, S. Lazar, S. Krinner, N. Lacroix, G. J. Norris, M. Gabureac, C. Eichler, and A. Wallraff. Repeated quantum error detection in a surface code. *Nat. Phys.*, 16:875–880, 2020.

[96] L. Ranzani, M. Bal, Kin Chung Fong, G. Ribeill, X. Wu, J. Long, H.-S. Ku, R. P. Erickson, D. Pappas, and T. A. Ohki. Kinetic inductance traveling-wave amplifiers for multiplexed qubit readout. *Appl. Phys. Lett*, 113(24):242602, 2018.

[97] B. Abdo, N. T. Bronn, O. Jinka, S. Olivadese, A. D. Córcoles, V. P. Adiga, M. Brink, R. E. Lake, X. Wu, D. P. Pappas, and J. M. Chow. Active protection of a superconducting qubit with an interferometric josephson isolator. *Nat Commun*, 10:3154, 2019.

[98] B. Abdo, O. Jinka, N. T. Bronn, S. Olivadese, and M. Brink. High-fidelity qubit readout using interferometric directional josephson devices. *PRX Quantum*, 2:040360, 2021.